DESIGN OPTIMIZATION OF AN S-SHAPED SUBSONIC INTAKE USING BAYESIAN APPROACH AND BEZIER CURVES

A THESIS SUBMITTED TO
THE GRADUATE SCHOOL OF NATURAL AND APPLIED SCIENCES
OF
MIDDLE EAST TECHNICAL UNIVERSITY

BY

METE ATASOY

IN PARTIAL FULFILLMENT OF THE REQUIREMENTS
FOR
THE DEGREE OF MASTER OF SCIENCE
IN
AEROSPACE ENGINEERING

MAY 2022

Approval of the thesis:

DESIGN OPTIMIZATION OF AN S-SHAPED SUBSONIC INTAKE USING BAYESIAN APPROACH AND BEZIER CURVES

submitted by **METE ATASOY** in partial fulfillment of the requirements for the degree of **Master of Science in Aerospace Engineering Department, Middle East Technical University** by,

Prof. Dr. Halil Kalıpçılar
Dean, Graduate School of **Natural and Applied Sciences** _____

Prof. Dr. Serkan Özgen
Head of Department, **Aerospace Engineering** _____

Prof. Dr. Yusuf Özyörük
Supervisor, **Aerospace Engineering, METU** _____

Examining Committee Members:

Prof. Dr. Dilek Funda Kurtuluş
Aerospace Engineering, METU _____

Prof. Dr. Yusuf Özyörük
Aerospace Engineering, METU _____

Prof. Dr. Sinan Eyi
Aerospace Engineering, METU _____

Assoc. Prof. Dr. Nilay Sezer Uzol
Aerospace Engineering, METU _____

Assoc. Prof. Dr. Munir Elfarra
Aerospace Engineering, Ankara Yıldırım Beyazıt University _____

Date: 26.05.2022

I hereby declare that all information in this document has been obtained and presented in accordance with academic rules and ethical conduct. I also declare that, as required by these rules and conduct, I have fully cited and referenced all material and results that are not original to this work.

Name, Surname: Mete Atasoy

Signature :

ABSTRACT

DESIGN OPTIMIZATION OF AN S-SHAPED SUBSONIC INTAKE USING BAYESIAN APPROACH AND BEZIER CURVES

Atasoy, Mete
M.S., Department of Aerospace Engineering
Supervisor: Prof. Dr. Yusuf Özyörük

May 2022, 75 pages

Engine is a prominent part for the systems of a cruise missile. Reliable and efficient engine performance significantly depends on the quality of the incoming airflow. In this thesis, the aerodynamic performance of a subsonic intake is improved by using open-source multi-task Bayesian optimization (MTBO) tool [1]. The main difference of Bayesian approaches from other optimization methods is that it has information about all design space, along with the uncertainty value. The learning process in the Bayesian approach is developed using the correlation of two different numerical methods. Also, machine learning-based optimization combined with multi-tasking used in this thesis is a pioneering work for air-intake design. The commercial computational fluid dynamics (CFD) solver ANSYS Fluent © is used to calculate the flow variables through the intake. The flow quality at a plane interfacing with the engine (denoted as the aerodynamic interfacing plane, AIP) are usually quantified with the flow uniformity and level of pressure loss. MTBO employs a Gaussian process with both high and low cost solutions for machine learning. Then, an acquisition function scores the system output of the surrogate model. In addition, turbulence model

selection studies for both cost levels are conducted. An objective function is utilized based on the weighted sum of non-dimensional values of Distortion Coefficient (DC), Pressure Recovery (PR) and weight of the S-duct. Initial sampling approach for multi-tasking approaches is also investigated. Multi-tasking is compared with single-tasking for total execution time when similar optima is achieved. Furthermore, parameters in the objective functions are investigated with Pareto plots.

Keywords: Subsonic Intake Optimization, Aerodynamics, Multi-Task Bayesian Optimization, Bezier Curve, Machine Learning

ÖZ

BAYES YAKLAŞIMI VE BEZİER EĞRİLERİ KULLANARAK S-ŞEKİLLİ SES-ALTI HAVA-ALIĞININ TASARIM OPTİMİZASYONU

Atasoy, Mete
Yüksek Lisans, Havacılık ve Uzay Mühendisliği Bölümü
Tez Yöneticisi: Prof. Dr. Yusuf Özyörük

Mayıs 2022 , 75 sayfa

Motor, seyir füze sistemleri için önemli bölümdür. Motor performansının güvenilir ve verimli olması önemli ölçüde ön yüzüne gelen havanın kalitesine bağlıdır. Bu tezde, açık kaynaklı çoklu görev tabanlı Bayes optimizasyonu ile bir ses altı hava alığının aerodinamik performansı iyileştirilmiştir [1]. Bayes yaklaşımının diğer optimizasyon yöntemlerinden temel farkı, belirsizlik değeri ile birlikte tasarım uzayındaki tüm hedef değerleri hakkında bilgi sahibi olmasıdır. Bayes yaklaşımındaki öğrenme süreci, iki farklı sayısal yöntemin korelasyonu kullanılarak geliştirilmiştir. Ayrıca, çoklu görevle birleştirilmiş makine öğrenimi tabanlı optimizasyon, hava alığı tasarımı için öncü bir çalışmadır. Hesaplamalı Akışkan Dinamiği çözücüsü ANSYS Fluent © hava-alığının akış performans parametrelerini hesaplamak için kullanılmıştır. Motorun ön yüz düzlemindeki (AIP) bir akışın performansı, akış homojenliği ve toplam basınç kaybı seviyesinden oluşur. Çok görevli Bayes özyineleme algoritmaları pahalı ve ucuz çözümlerle Gauss Süreçlerini uygulayarak modellemeye çalışır. Ayrıca, edinme işlemi vekil modelin sistem çıktısını puanlar. Ek olarak, her iki doğruluk seviyesi için türbülans modeli seçim çalışması yapılmıştır. Hedef fonksiyonu bozuntu

katsayısı(DC60), basınç geri kazanımı (PR) ve model ağırlığının boyutsuzlaştırılmasıyla oluşturulmuştur ve eşit ağırlıklandırma ile tanımlanmıştır. Başlangıç eleman sayılarının özyineleme yönelimi üzerindeki etkisi incelenmiştir. Çoklu görev yaklaşımı toplam tasarım süresi bakımından tekli görev yaklaşımı ile kıyaslanmıştır. Ayrıca hedef fonksiyonun içerisindeki parametreler arasındaki ilişkiler çoklu pareto grafikleri ile incelenmiştir.

Anahtar Kelimeler: Ses-altı Hava Alığı Optimizasyonu , Aerodinamik, Çok Görevli Bayes Optimizasyonu, Bezier Eğrisi, Makine Öğrenmesi

To my love

ACKNOWLEDGMENTS

I would like to acknowledge and give my warmest thanks to my supervisor Prof. Dr. Yusuf Özyörük who made this work possible. His guidance and advice carried me through all the stages of my thesis.

I'd also like to express my gratitude to my colleagues at Roketsan's Aerodynamics Division for all of their assistance and support throughout the thesis. I want to express my best wishes to Mr. Ertan Demiral, Mr. Erdem Dinçer, Mr. Efe Can Dağlı and Mr. Tezcan Ünlü for their friendship and support during this study.

I would like to thank my friends, Mr. Osman Güngör, Mr. Özgün Savaş and Mr. Ali Oğuz Yüksel for their help and motivation.

Finally, I would also like to give special thanks to my wife Mrs. Esra İçen Atasoy and my daughter Nil Atasoy for their continuous support and understanding when undertaking my research and writing my thesis.

TABLE OF CONTENTS

LIST OF TABLES

TABLES

LIST OF FIGURES

FIGURES

LIST OF ABBREVIATIONS

ABBREVIATIONS

α	Angle of Attack
β	Angle of Side-slip
$\dot{m}$	Mass Flow Rate
ρ	Air Density
R	Gas Constant
Q	Dynamic Pressure
AIP	Aerodynamic Interface Plane
CFD	Computational Fluid Dynamics
DC	Distortion Coefficient
GP	Gaussian Process
M	Mach Number
MTBO	Multi Task Bayesian Optimization
P_t	Total Pressure
PDE	Partial Differential Equations
ARANS	Averaged Reynolds Averaged Navier-Stokes
RAE	Royal Aircraft Establishment
RANS	Reynolds Averaged Navier-Stokes
RMSE	Root Mean Square Error
RHS	Right Hand Side
PR	Pressure Recovery
PRA	Static Pressure Ratio
TM	Turbulence Model

CHAPTER 1

INTRODUCTION

Cruise missile is an efficient way of deploying large warheads for long distance targets with high precision capability. Most cruise missiles work with relatively small air-breathing turbojet engines. The classification of a cruise missile is determined by its range, size and speed [5],[13]. These classification parameters affect turbojet engine selection for a cruise missile. Even the overall performance of a missile is determined mostly by the engine capability. Engines are comprised of various parts and subsystems. In turbojet engines, air intakes, sometimes referred as inlets, let free-stream air flow into the engine.

1.1 Problem Definition

Intake geometry design is quite important for the aerodynamic performance of a cruise missile. It is essential to have the incoming air at appropriate conditions, with the least possible loss in terms of flow quality. Intake geometries are specialized for almost every air-breathing missile types. For cruise missiles, S-shaped geometries are prominent since ambient flow should be canalized from the outside to the center of the interface plane of an engine [3].

Determining the flow variables through the subsonic S-shaped intake is quite challenging for designers since the flow there usually is highly complex in structure. Flow simulations are mostly performed by using computational fluid dynamics (CFD) by numerically solving the Navier-Stokes equations [14], since experimental research is very costly, requiring huge amounts of power [15], equipment and preparation time. For this reason, numerical applications are used in this thesis.

Figure 1.1: Example of a Cruise Missile [3]

Another difficulty for design of S-shaped intakes is associated with incorporating efficient optimization. Lots of geometry input parameters, objectives and constrains for intakes make any design optimization difficult in terms of level of accuracy and solution time.

1.1.1 Intake Flow Physics

Flows in S-duct are quite complicated for certain reasons. When the flow passes through the subsonic intake, vortex generation or secondary flow takes place. The S-shape bends the flow and that changes the inner flow characteristics causing a formation of losses. To assess the quality of the flow that enters the engine, pressure recovery (PR) and distortion coefficient (DC) are the two most commonly inspected performance parameters. The level of PR losses through an intake is determined greatly by the levels of wall friction, flow separation and shock waves [16]. The second parameter, namely DC, is an indicated to the level of flow non-uniformity at interfacing plane to the engine. Secondary motions and boundary layer development have quite an impact on this parameter.

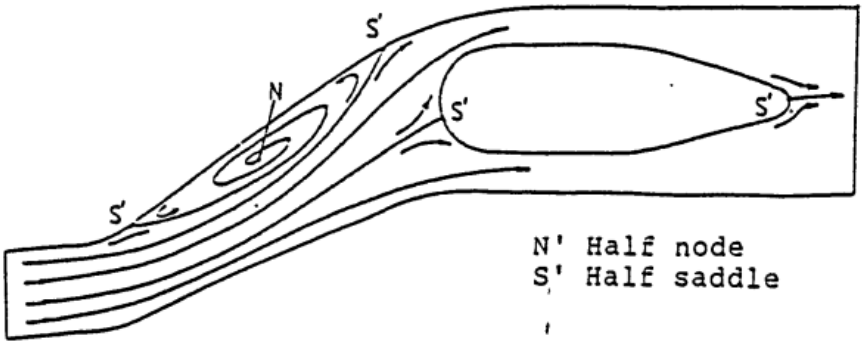

Figure 1.2: An Example of a Flow Pattern of S-duct [4]

In an S-shaped duct, the first bend generates the secondary motions of flow which may end up with flow separation. Then, some viscous region follows and total pressure losses build further around the second bend [4]. These complex structures should be well resolved for design optimization applications.

1.1.2 Applications of Intake Flow Analysis

There appear many studies in literature that investigated flows through subsonic intakes numerically and experimentally [17]. Though, the most of these are numerical since the experimental ones are more expensive than computer based applications and experimental research can require huge amounts of power for operation. The power requirement of a wind tunnel depends mainly on test chamber cross-section, flow Mach number and Reynolds Number [15]. On the other hand, determining the flow variables is challenging for numerical applications since flow is usually highly turbulent especially through S-shaped ducts. Finding the flow variables through an intake by solutions to the Navier-Stokes equations is a common approach[18],[19]. Directly solving governing equations with performing Direct Numerical Simulation (DNS) means to solve the all persisting eddies. However, the total number of meshes for DNS depends on the flow Reynolds number ($\approx Re^{9/4}$) [20]. That makes DNS almost impossible to be used for most engineering problems. In a situation where DNS is not applicable, some modifications to the governing equations are implemented [21].

The Reynolds Averaging method is used in the majority of CFD simulations to obtain an approximate averaged solutions to the Navier–Stokes equations. However, averaging of Navier-Stokes equations yields a nonlinear Reynolds stress term that requires additional modeling to fully resolve the system. In order to solve Reynold Averaged Navier-Stokes (RANS) equations, Boussinesq hypothesis was proposed to create an idea that turbulent eddies can be calculated with the assumption of eddy viscosity formulation [22]. Then, the turbulence models differ from the assumption of turbulent eddy viscosity in the Reynolds stress tensor. The various models (like algebraic, one equation, two equation etc.) are derived to represent the effect of the turbulence. Although one equation turbulence model Spalart–Allmaras (SA) is proposed for special aerospace application [23], it is rarely used for duct flow [16]. Indeed, some variations of k-ϵ and k-ω turbulence model are widely applied to investigate the flow fields of an air intake [24],[12]. Detailed information about turbulence modelling is presented in the following chapter.

1.1.3 Shape Optimizations for Intake Design

An optimization implies meticulously selecting input values from within an acceptable set and computing the value of a function to maximize or minimize. With breakthroughs in computing technology and a growing attention on optimization techniques, there have been numerous innovative approaches. In shape optimization problems, the aim is to improve the performance of the structure by modifying its boundaries. Types of optimization techniques used for geometry design are briefly explained as follows,

- Gradient descent is an optimization technique for finding the minimum of an objective function by following the function's negative gradient. It is a straightforward approach that can be used in shape optimization. The direction of gradient-based progress is influenced by the starting points and first order iterative progress can have a problem for those whose objective function has multiple local optima [25]. Even, gradient based optimizations may get stuck when dealing with high-dimensional nonlinear optimization problems with several local optima.

- In stochastic optimization, the objective function incorporates randomness. The randomization of a stochastic optimization approach does not imply that the application is entirely random [26]. More specifically, in order to prevent these algorithms from getting stuck of local optima unlike gradient based [27], certain level of randomness is considered. However, they are very slow when the input size of the system is large.

- Surrogate models have been recently used in complex engineering design to replace expensive simulations or physical experiments. A surrogate model builds a statistical model to approximate the simulation outcome accurately. The original computer simulation can be replaced with this statistical model by applying sensitivity analysis, optimizations, or risk analysis [28]. Data analysis is used to train a surrogate model. Then, a single evaluation of the original simulation takes substantially longer than a single evaluation of the trained statistical model. Polynomial regressions, Gaussian Processes, neural networks, etc., are examples of the surrogate models. Bayesian Optimization is widely used as a surrogate based optimization method for many engineering problems. It makes use of Bayes' Theorem to guide an efficient search for a global optimization issue [29].

1.2 Literature Survey

Thanks to the technological development in air power in the 1940s, a cruise missile concept was introduced in many army's inventory. Mission capabilities of cruise missiles cannot be executed by most classical weapons. Since there were many different requests of mission from the authorities in the past, a new concept of air-breathing missiles came out. The cruise missile spends the majority of its flight trajectory under cruise conditions, which means it maintains a constant altitude and speed. Sahm and Werrell [5] investigated chronologically the evaluation of cruise missiles trying to point out whether cruise missile technology was a milestone. Firstly, they also noted that Germans found first "Flying Bombs" namely V-1 which is powered by a pulse

jet engine.

Figure 1.3: German V-1 Flying Bomb (Imperial War Museum)[5]

There are many experimental and numerical studies about intake flow. In 1992, Harloff [30] performed an experimental analysis of S-duct at NASA Lewis Research Center to test the solution of the three dimensional Navier Stokes based flow solver. In order to validate their in-house code, PARC3D, algebraic and k-ϵ turbulence models are used. Their study reveals that both turbulence model don't perform well for strong secondary flows with separation. Moreover, Royal Aircraft Establishment (RAE) subsonic intake model M-2129 [31] is used as a validation case in common by a great amount of research. Aref used that S-shaped model to test their CFD methodology [16]. It is states in their study that Hybrid DDES numerical method performs better than RANS models and Spalart-Allmaras, one equation turbulence model, don't capture smaller vorticities as well. Detached Eddy Simulations were first introduced at the study of Spalart [23],[32]. The Hybrid DDES turbulence model requires finer grid resolution than RANS simulation[33].

There are several studies about aerodynamic performance of an intake in literature [34], [35]. In Wellborn's study [36] total pressure, static pressure and velocity fields are collected at five cross-sections of a S-duct to visualize separately the behavior of flow variables. From contours of pressures, separation is clearly seen at the lower part of S-duct since the counter-rotating vorticities induced by a duct curvature causes the flow to lose momentum. Distortion coefficient is an another performance parameter of an intake to be investigated by the various study. It is defined as the difference between worst total pressure among 60^0, any worst of 4 pieces of 15^0 at AIP, averaged total pressure divided by dynamic pressure of location at the engine face [37],[38].

Zhang and Vahdati [39] examine the detrimental effects on compressor blades due to the distortion of incoming flow by the using of AU3D flow solver. Instantaneous velocity profiles of the rotor section in their study are visualized for each stage and tip vortex triggered the periodical stall through the compressor. There have been many trade-off studies for weight and performance. Thrust requirement defines the cruise missile size since higher thrust is produced by a large engine. Thrust to weight ratio is essential performance parameters for fixed wing air-platforms [40].

Mathematical descriptions of geometries are involved in many design optimization literature researches. Curvatures in a specific geometry can be defined by polynomials and splines. Hicks and Henne [41] introduced a bump function for airfoils. The amplitude, the location and the height of the bump functions for each curve defines the shape. Bezier curve is an another function proposed by Pierre Bézier [6], French engineer doing external body design for Renault™. It is also called as a Bernstein-Bezier curve because of its close relation to Bernstein function.

Optimization methodology is used for many fields of science to solve a variety of specific problems. There are mainly many types of method for searching techniques, which are stochastic, gradient based and surrogate based. Gradient based searching entails by computing the slope using the entire data set or preparation set in order to find the best arrangement [42], [43]. In 2014, Oral [44] uses gradient based optimization on parametric submerged intake geometry to find optimum design point . Approaches for optimum solution are direct, each cycle involves going over the full data set. Also, a lot of computational effort and time are required for the non-linear problems since gradient based can be lingered around locals. Stochastic methods, on the other hand, enable alternate approaches by allowing for fewer choices to be taken into the search with certain randomness. In 1996, Mitchell [45] proposed an optimization algorithm related to Darwin's Evaluation Theory. Progress of initially random samples are applied to crossover and random mutation with respect to their fitness. Each sample has its own encoding of chromosome representation [46]. Kennedy and Eberhart [47] introduced the Particle Swarm Optimization (PSO) method in 1995 for non-linear continuous functions. Theory behind the PSO is that all particles move around space and share their position and velocity information . All stochastic optimization methods have some degree of sensitivity to the size of the initial population

[27].

Bayesian optimization had been introduced by a series of Mockus'work [48],[49], [50]. Bayesian approximation is based on the Bayes Theorem, which states that the probability of an event is conditional. It uses a surrogate function to model surface for design input with its objective values. Moreover, the Gaussian Process is widely used for computationally expensive problems as a surrogate function. Then, the acquisition function predicts the candidate design points which have good performance. Kennedy and Hagan [51] performed a Gaussian Process with linear multi-fidelity model for their specific multi-level computer code. They claim that the elapsed time for estimated data was significantly less than that of expensive runs using Bayesian Methods. In addition, Perdikaris [52] uses multi-fidelity modelling for multi-fidelity modelling using GPs. They emphasize that it is possible to have erroneous in the predictions if there is a poor correlation between these two different ranked fidelities. Huang [53] introduced in 2006 a new method optimization named the Multiple Fidelity Sequential Kriging optimization. Due to the higher computational cost, lower fidelity results are used by a kriging meta-model to predict higher fidelity results. Furthermore, different fidelities of solution are combined to find any correlations and this correlation helps to estimate the results from expensive methods. Surrogate model is established with all available data which involve expensive data and corrected cheap data. Swersky [8] uses multi-fidelity Bayesian optimization. The basic idea of this technique is to apply a multi-task Gaussian process with Bayesian optimization. Main difference of multi-task Bayesian optimization (MTBO) with standard task approach is that surrogate function is constituted with mixing more than one fidelity of solution techniques. Letham and Baksky [54] studied online-offline experimentation of Bayesian Optimization. To sum up, their study provides mean values prediction error for online, offline and MTBO predictions. MTBO performs outstanding convergence rate compared to the others and they pointed out the single task model failure on their experiments.

1.3 Thesis Objectives

The objective of the thesis is to develop effective design approaches for subsonic intake shape optimization by applying multi-task Bayesian optimization. In order to reduce the amount of computationally expensive tasks, a machine learning based design optimization is used to show that Bayesian approach with multi-tasking can be applicable for intake design problems. Giving an alternative engineering approach to the geometrical representation for subsonic intakes is an another objective of thesis. After setting certain design points for the surrogate model, its predictive ability is tested with missing data. Multi-tasking optimizations with different sizes of initial sampling are conducted to show their final design outcome. The fitness scores of these approaches with different initial samplings are expected to be similar. Also, using two different costs of solutions on Bayesian optimization is expected to lower optimization time. Finally, the performance parameters of an intake model are investigated with Pareto plots to better visualize the relations.

1.4 Outline of the Study

In Chapter 1, brief information on cruise missile and their intake performance is provided. Then, main problems and breakthroughs to their solutions are addressed. Literature review of numerical application and optimization details are given and up-to-date situation and applications are mentioned.

Chapter 2 provides the details of the formulation governing equations and mathematical applications on intakes and branches of Bayesian optimization required to support methodology. Then, the details of performance parameters are provided.

Results and discussions for validation cases are included in Chapter 3. Numerical applications and performance comparison with available data are mentioned in figures and contour plots.Then, chapter 4 gives the multi-task optimization outcomes with respect to different numbers of initial sampling with cross validation, task comparison and parameters relation in the objective function.

Chapter 5 concludes the thesis with gains and outcomes related MTBO.

CHAPTER 2

METHODOLOGY

Numerical flow solutions that are needed by the optimization procedure are obtained by solving the Reynolds-Averaged Navier-Stokes (RANS) equations with various turbulence models. Geometric optimization fed by these solutions is carried out using a multi-task Bayesian optimization (MTBO) method. In this chapter, the flow solver with the employed turbulence models is described first. Then, the MTBO method is detailed. The solved subsonic intake problem is also discussed in detail. Also, sampling technique is explained. After that, the geometrical description of S-shaped duct will be explained. Finally, objective function used in Bayesian optimization will be given as a summation of normalized values of distortion coefficient, pressure recovery and weight of S-shape.

2.1 Governing Equations

The mathematical descriptions that constitute the framework of a computational algorithm are referred to as the governing equations. For Computational Fluid Dynamics (CFD), fluid motion is described by conservation of mass, momentum and energy. In the present study the conservation equations are solved employing the commercial ANSYS Fluent © [55] software. For completeness, they are included also here.

The conservation of mass equation is given as,

$$\frac{\partial \rho}{\partial t} + \frac{\partial (\rho u_i)}{\partial x_i} = 0 \tag{2.1}$$

where ρ is the density of the fluid and u is the velocity.

The conservation of momentum equations are given below:

$$\frac{\partial(\rho u_i)}{\partial t} + u_j \frac{\partial(\rho u_i)}{\partial x_j} = -\frac{\partial p}{\partial x_i} + \frac{\partial \tau_{ij}}{\partial x_j} + \rho g_i \tag{2.2}$$

where p is the pressure of the fluid, τ_{ij} is the shear stress term and g_i is the gravity.

With Newtonian assumption which stated that viscosity is not affected by shear rate, the stress tensor formulated as follows.

$$\tau_{ij} = 2\mu S_{ij} + \lambda \frac{\partial v_k}{\partial x_k} \delta_{ij} \tag{2.3}$$

where δ_{ij} denotes the Kronecker delta, μ denotes the viscosity and λ denotes dynamic viscosity of the fluid. In shear stress term, μ is calculated by using Sutherland's law to consider the temperature effects on dynamic viscosity.

$$\mu = \mu_0 \left(\frac{T}{T_0}\right)^{3/2} \left(\frac{T_0 + 110.56}{T + 110.56}\right) \tag{2.4}$$

where μ_0 is 1.716$\times$ 10^{-5} in kg/m-s and T_0 is 273.11 in K.

The RHS of momentum equations consists of all the force terms such as shear, surface and body. The equation of thermal energy is given as

$$\frac{\partial(\rho h)}{\partial t} + \frac{\partial(\rho h u_i)}{\partial x_i} = \frac{\partial}{\partial x_i}\left(k \frac{\partial T}{\partial x_i}\right) + S \tag{2.5}$$

where k is the thermal conductivity coefficient, h denotes the total enthalpy and S is the heat dissipation term.

The Navier-Stokes equations are coupled and should be solved simultaneously. There are 6 flow variables for three dimensional compressible analysis to be calculated but the Navier-Stokes equations consist of 5 conservation equations. Due to compressibility of flow, pressure is obtained with perfect gas assumption which allows equation of state to close the system.

$$P = \rho R T \tag{2.6}$$

where R denotes gas constant and T denotes the static temperature.

2.2 Reynolds-Averaged Navier-Stokes Equations

Osborne Reynolds [21] proposed Reynolds decomposition for the flow parameters, which splits the instantaneous values into average and fluctuation components; for example for the x-velocity into $\bar{u}$ and u', respectively. Reynolds decomposition simplifies the governing equations. After introducing the Reynolds decomposition into the N-S equations, terms like $\rho\overline{u'v'}$ appear in the averaged momentum equations. These terms are related to the eddy viscosity concept associated with turbulence.

$$\tau_{ij}^{R} = -\rho\overline{u'v'} = 2\mu_T\overline{S_{ij}} - \frac{2}{3}\rho K\delta_{ij} \tag{2.7}$$

where δ_{ij} denotes the Reynolds-averaged strain-rate tensor, K denotes the turbulent kinetic energy. There is a closure problem for the RANS equations with these additional terms since the number of equations is not altered while the unknowns now include the fluctuating parts. To satisfy the system of equations, the Boussinesq hypothesis [56] has been used to model the turbulent quantities. Boussinesq assumption is based on the idea that there is an extra dissipation term, which is isotropic, created by turbulent stresses. The classification of eddy viscosity models comes from the formulation and approximation of turbulent viscosity terms in Reynolds stresses. The linear eddy viscosity models are divided into following groups;

- Algebraic Models (No models)
- One Equation Model (Spalart-Allmaras Model, Prandtl's Model, etc.)
- Two Equation Model (SST-k-ω, Realizable k-ϵ,etc.)

In this thesis, the Spalart-Allmaras one equation, and realizable k-ϵ two equation turbulence model are used for the low and high fidelity numerical flow solutions as required by the optimization approach employed in the thesis. These turbulence models are discussed below.

2.2.1 Spalart-Allmaras Turbulence Model

The Spalart-Allmaras turbulence model uses a single transport equation to determine the eddy viscosity ν term . The model was developed primarily for aerodynamic and

turbomachinery applications related to wall-bounded flows. Despite a large number of parameters and coefficients included in the kinematic equation, it is substantially less computationally intensive than of course direct simulation technique. In addition to this, to determine a turbulent length scale, the shear layer thickness does not need to be adjusted locally. Also, the Spalart-Allmaras turbulence model has an excellent prediction capability for turbulent flows with adverse pressure gradients.

The Spalart-Allmaras turbulence model formulation [23] given in tensor notation as follows

$$\begin{aligned}\frac{\partial \bar{\nu}}{\partial t} + \frac{\partial(\bar{\nu} v_j))}{\partial x_j} &= C_{b1}(1 - f_{t2})\bar{S}\bar{\nu} \\ &+ \frac{1}{\sigma}\left\{\frac{\partial}{\partial x}\left[(\nu_L + \bar{\nu})\frac{\partial \bar{\nu}}{\partial x_j})\right] + C_{b2}\frac{\partial \bar{\nu}}{\partial x_j}\frac{\partial \bar{\nu}}{\partial x_j}\right\} \\ &- \left[C_{w1} f_w - \frac{C_{b1}}{\kappa^2} f_{t2}\right]\left(\frac{\bar{\nu}}{d}\right)^2 + f_{t1}\left\|\Delta \vec{v}\right\|_2^2\end{aligned} \tag{2.8}$$

The eddy viscosity production terms are given as below

$$\bar{S} = f_{v3} S + \frac{\bar{v}}{\kappa^2 d^2} f_{v2} \tag{2.9}$$

where S is the magnitude of the mean rotation rate.

$$f_{v1} = \frac{\chi^3}{\chi^3 + C_{v1}^3}, \quad f_{v2} = \left(1 + \frac{\chi}{C_{v2}}\right)^{-3} \tag{2.10}$$

$$f_{v3} = \frac{(1 + \chi f_{v1})(1 - f_{v2})}{max(\chi, 0.001)}, \quad \chi = \frac{\bar{\nu}}{\nu} \tag{2.11}$$

$$S = \sqrt{2\Omega_{ij}\Omega_{ij}} \tag{2.12}$$

The laminar-turbulent transition terms are defined as

$$f_{t1} = C_{t1} g_t exp\left(-C_{t2}\frac{w_t^2}{\Delta U^2}(d^2 + g_t^2 d_t^2)\right) \tag{2.13}$$

$$f_{t2} = C_{t3} exp(-C_{t4}\chi^2), \quad g_t = min\left[0.1, \left\|\Delta \vec{v}\right\|_2 / (w_t \Delta x_t)\right] \tag{2.14}$$

where ω_t represents the vorticity at the wall at the trip point, $\Delta\vec{v}_2$ denotes the 2-norm of the difference between the velocity at the trip point and the current field point, d_t is the distance to the nearest trip point, and Δx_t stands for the spacing along the wall at the trip point.

Finally, the constant parameters in the Spalart-Allmaras equation are defined as

$$C_{b1} = 0.1355, \qquad C_{b2} = 0.622$$
$$C_{v1} = 7.1, \qquad C_{v2} = 5, \qquad \sigma = 2/3, \qquad \kappa = 0.41$$
$$C_{w1} = C_{b1}/\kappa^2 + (1 + C_{b2})/\sigma, \qquad C_{w2} = 0.3, \qquad c_{w3} = 2$$
$$C_{t1} = 1, \qquad C_{t2} = 2, \qquad C_{t3} = 1.3, \qquad C_{t4} = 0.5$$

2.2.2 Realizable k-ϵ Turbulence Model

The k-ϵ model was founded firstly for free-shear layer flows with small pressure gradients, such as free jets. The equation dynamics of the Realizable k-ϵ turbulence models is similar to the original version of the k-ϵ turbulence model. The turbulent kinetic energy k and the rate of dissipation of the turbulent energy ϵ defines the two equation approaches to model turbulence mechanism. Due to insufficiency of the k-ϵ model for flows with adverse pressure gradients, there have been many modified versions of the transport-diffusion equations [57],[58]. An alternative to the turbulent viscosity formulation of the standard k-ϵ turbulence model, the so-called realizable k-ϵ turbulence model was introduced by Shih [59] for high Reynolds number turbulent flow. An exact version of the equation for the transfer of the mean-square vorticity fluctuation was reformulated as a dissipation rate equation. Indeed, the model's ability defines the realizable version satisfying specific mathematical expressions on the Reynolds stress term for turbulent flows. The main difference between the realizable k-ϵ and the standard version comes from the definition of an eddy-viscosity formulation and derivation of the mean-square vorticity fluctuation.

The eddy viscosity is given as follows

$$\mu_t = \rho C_\mu \frac{k^2}{\epsilon} \tag{2.15}$$

For a new method C_μ is not constant as in Re-Normalize Group (known as RNG) k-ϵ turbulence model

$$C_\mu = \frac{1}{A_0 + A_s \frac{kU^*}{\epsilon}} \tag{2.16}$$

The model constants A_0 and A_s are given as

$$A_0 = 4.04, A_s = \sqrt{6} cos(\phi) \tag{2.17}$$

where

$$\begin{aligned} \phi &= \frac{1}{3} cos^{-1}(\sqrt{6} W) \\ W &= \frac{S_{ij} S_{jk} S_{ki}}{\tilde{S}^3} \\ \tilde{S} &= \sqrt{S_{ij} S_{ij}} \\ Sij &= \frac{1}{2} \left(\frac{\partial u_j}{\partial x_i} + \frac{\partial u_i}{\partial x_j} \right) \end{aligned} \tag{2.18}$$

U^* is another parameter in the model and formulation are given as

$$U^* = \sqrt{S_{ij} S_{ij} + \widetilde{\Omega}_{ij} \widetilde{\Omega}_{ij}} \tag{2.19}$$

where

$$\begin{aligned} \widetilde{\Omega}_{ij} &= \Omega_{ij} - 2\epsilon_{ijk} w_k \\ \Omega_{ij} &= \overline{\Omega}_{ij} - \epsilon_{ijk} w_k \end{aligned} \tag{2.20}$$

where $\overline{\Omega}_{ij}$ is the mean rate-of-rotation tensor viewed in a rotating reference frame with the angular velocity w_k

2.2.3 SST k-ω Turbulence Model

The Shear-Stress Transport k- ω model was formulated out in 1994 by Menter [60] to be used as the inner part of boundary layer directly. It is a two-equation eddy viscosity model and combination of Standard k-ϵ and Wilcox's k-ω turbulence models. The standart k-ω model is applicable for low Reynolds number flows. Flow has thicker boundary layer at low Reynolds numbers since viscous terms are dominant. The SST k-ω turbulence models give good prediction capability for adverse pressure gradient and separating flow. However, there is a low prediction capability on where higher velocity gradients occur.

The governing equations for the SST k- ω model are given as follows,

$$\frac{\partial(\rho k)}{\partial t} + \frac{\partial(\rho k u_i)}{\partial x_i} = \frac{\partial}{\partial x_j}\left(\Gamma_k \frac{\partial k}{\partial x_j}\right) + \tilde{G}_k - Y_k + S_k \tag{2.21}$$

and

$$\frac{\partial(\rho w)}{\partial t} + \frac{\partial(\rho w u_i)}{\partial x_i} = \frac{\partial}{\partial x_j}\left(\Gamma_w \frac{\partial}{\partial x_j}\right) + G_w - Y_w + S_w + D_w \tag{2.22}$$

where $\tilde{G}_k$ denotes the turbulence kinetic energy generated by mean velocity gradients, G_w denotes the specific rate of dissipation, Γ is the effective diffusivity, Y represent the turbulence dissipation, D_w denotes the cross-diffusion and S are defined as a source.

2.3 Geometrical Description

Model geometry is defined by S-shape , lip and engine intake parts with bullet. Only S-shape geometrical representation is optimized. Initial points of Bezier are fixed with the center since it is important that there cannot be discontinuous in the control volume. Distance between input points $x_0, x_1, x_2, ...etc.$, are identical and length of duct defines each distance. The heights $y_1, y_2, ...y_6$, are changed in their limits and y_0 and y_7 are fixed with the location of front-end and back-end of S-duct respectively.

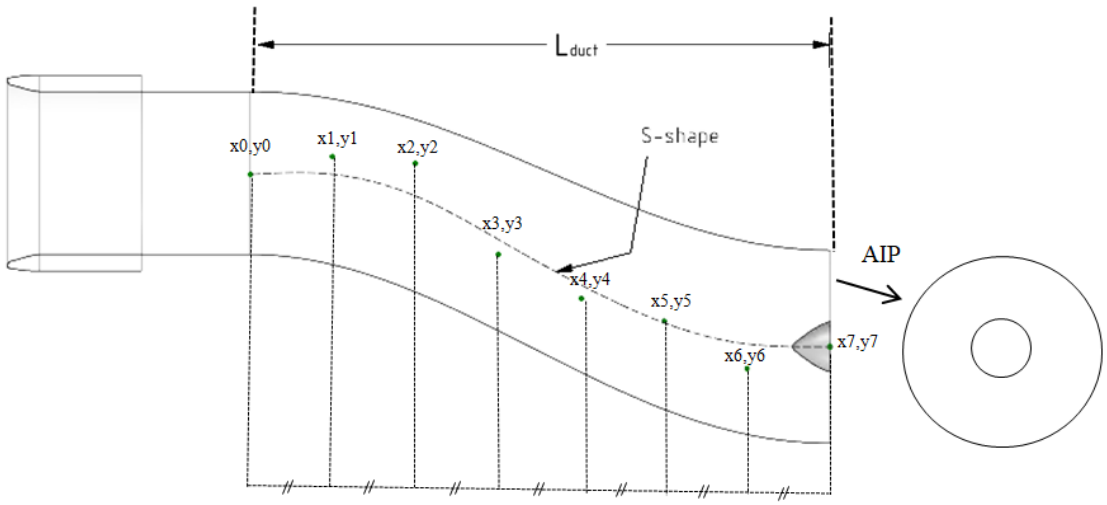

Figure 2.1: Geometric Parameters of S-Shape

Coordinate details of S-shape are provided in Figure 2.1. y_1 and y_6 should be carefully

selected for the line continuity.

$$(x_{i+1} - x_i) \mid_{i=[0,6]} = L_{duct}/n \qquad n \in [0, 7] \tag{2.23}$$

2.3.1 Bezier Curve

Bézier curves are used in many fields of computer aided technology. Two ends of points are stationary and between these points defines the curve. Moreover, the theory behind the Bezier curve is that it is a parametric curve defined by a set of control points. The Bezier curve defined by these points is defined and examples of Bezier curves are given in Figure 2.2.

$$P(t) = \sum_{i=0}^{b} B_i^n(t) \cdot P_i \qquad t \in [0, 1] \tag{2.24}$$

where $B(t)$, Bernstein polynomial given as

$$B_i = \begin{pmatrix} n \\ i \end{pmatrix} t^i (1-t)^{n-i}, \begin{pmatrix} n \\ i \end{pmatrix} = \frac{n!}{i!(n-i)!}$$

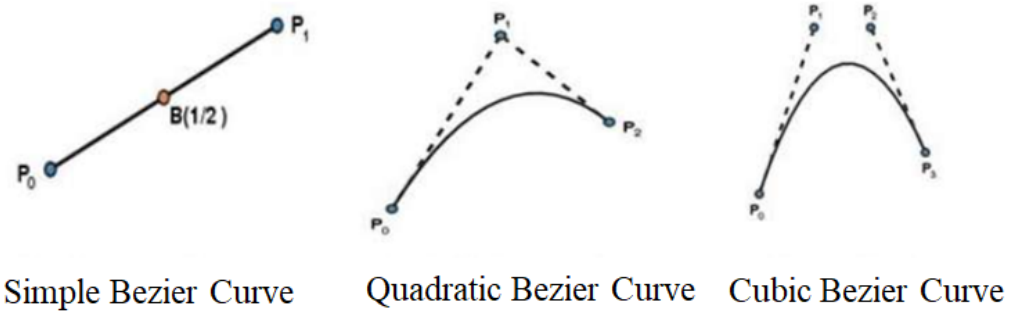

Figure 2.2: Bezier Curve Examples [6]

2.4 Design Optimization

This section explains the basic optimization concepts used in the design of the subsonic intake geometry in this thesis. When the number of input parameters is large, efficient searching strategies are required to lower the computational time. Large

grid/mesh size and higher order numerical applications are needed for complex flows to be solved accurately. These implementation are expensive and time-consuming application. When expensive analyses are required, surrogate modelling approaches are highly beneficial in engineering design. The surrogate based optimization consists of constructing a surface function and finding best scores from the mapped high-fidelity objectives data. Below stages of surrogate-based optimization approach are discussed in detail, together with their features and model functions.

2.4.1 Bayesian Optimization

Bayesian optimization is a method for determining the minimum or maximum of an objective function using the basis of Bayes' theorem. Bayesian optimization is the best for objective functions that are to evaluate costly [61].

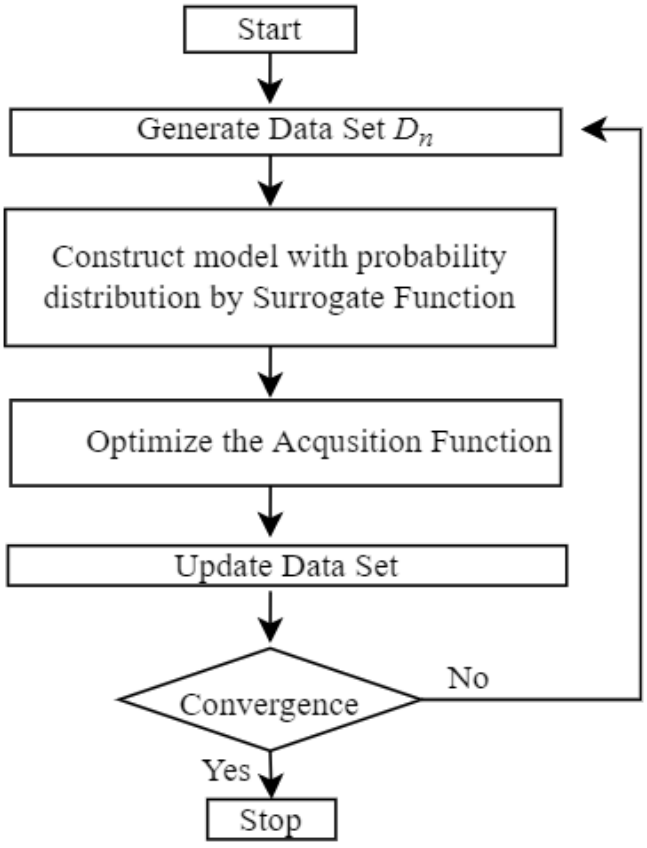

Figure 2.3: Flow Chart of Pseudo-Bayesian Optimization

The schema of the Bayesian optimization loop is given in Figure 2.3. In Bayes theorem , the posterior probability is related to the conditional probability. Starting to assess the space's, the theorem uses statistical models, generally Gaussian process, by providing posterior probability distribution to model potential values for objective function. Every iteration for Bayesian optimization, the statistical or surrogate model is updated. Then, acquisition function quantify the values of evaluation of the objective function and select the possible solutions to examine. The cycle is repeated until convergence is achieved.

2.4.1.1 Gaussian Process

A Gaussian process (GPs) is a set of functions with probability of a distribution. Many applications of GPs have been applied for regression analysis, dimension reduction and mapping of the function. A response surface model is illustrated by Gaussian kernel function , generally Radial Basis Function (RBF). A regression method is a simple way of learning relationship from inputs to outputs and it is a core technique for many statistical problems. The GPs is formulated as a combination of the mean function $\mu\left(f(x)\right)$ and a covariance function $K\left(f(x), f(x')\right)$.

$$
\begin{aligned}
f &\sim GP\left(\mu\left(f(x)\right), K\left(f(x), f(x')\right)\right) \\
\mu\left(f(x)\right) &= \mathbb{E}\left[f(x)\right] \\
K\left(f(x), f(x')\right) &= \mathbb{E}\left[(f(x) - \mu(x))(f(x') - \mu(x'))\right]
\end{aligned}
$$

Covariance identifies the correlations between input parameters in the space. Covariance matrix is always positive and symmetric. There are many types of covariance functions. The Radial Basis Function was introduced by Rasmussen and Williams [62] and it is defined the squared exponential kernel. That function is a prominent kernel used in the Gaussian process providing a smooth probability function. However, Matern kernel is used in the open source multi-task Bayesian optimization.

$$
K\left(f(x), f(x')\right) = \tau^2 exp\left(-\frac{1}{2}\sum_{j=1}^{N}\left(\frac{x_j - x'_j}{l_j}\right)^2\right) \tag{2.25}
$$

τ and l_j are two hyperparameters that define the capability of modeling the posteriors in terms of amplitude and length scale of variation. Following Figure 2.4 gives an example of a regression analysis by using an RBF based Gaussian process.

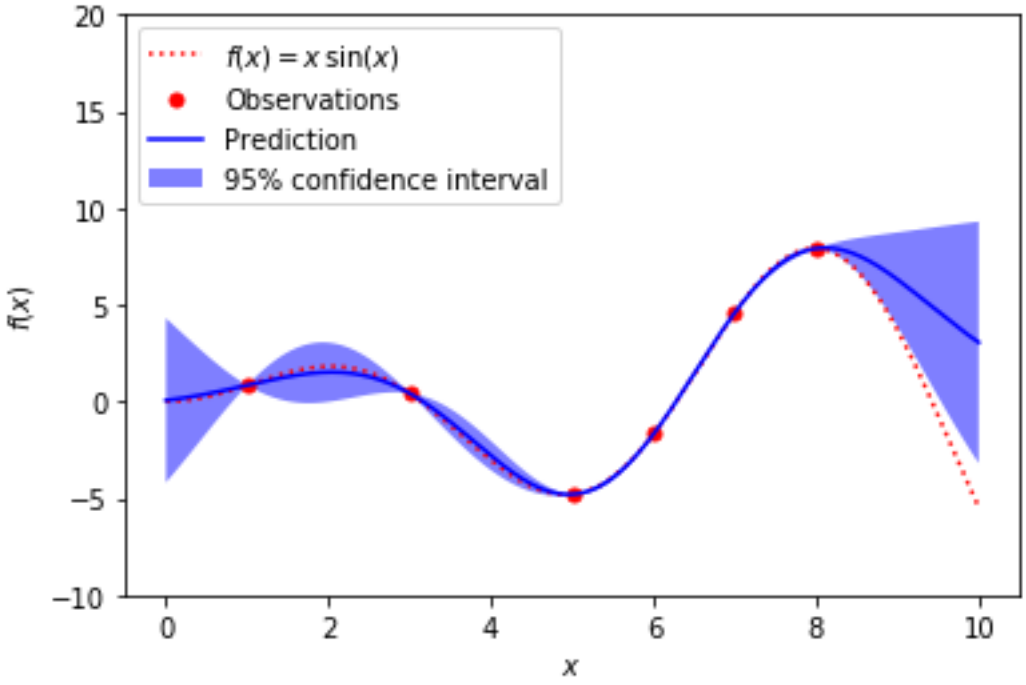

Figure 2.4: Example of a Gaussian Process [7]

2.4.1.2 Multi-Task Gaussian Process

A new approach for Gaussian process application was proposed by Swerky [8]. Covariance formulation was modified in his study to use different fidelity sets of applications. The reason for a number of fidelities usage is to make fast approximations due to limitations on resources and time. In other words, the system of domain can be modeled in a much less time with mixed fidelity approximation for computationally extensive problems. Covariance function of Multi-Task Gaussian Process (MTGP) models posteriors from all observations modeling high fidelity observation from low fidelity observation.

$$K_{MTGP}\left((x,t),(x',t')\right) = K_t(t,t') \otimes K_X(x,x') \tag{2.26}$$

where $\otimes$ refers Kronecker product, K_x defines the input correlation and K_t relates the task level.

Figure 2.5 shows Gaussian process over different fidelities. Correlation among tasks reduces global uncertainty in the multi-tasking application.

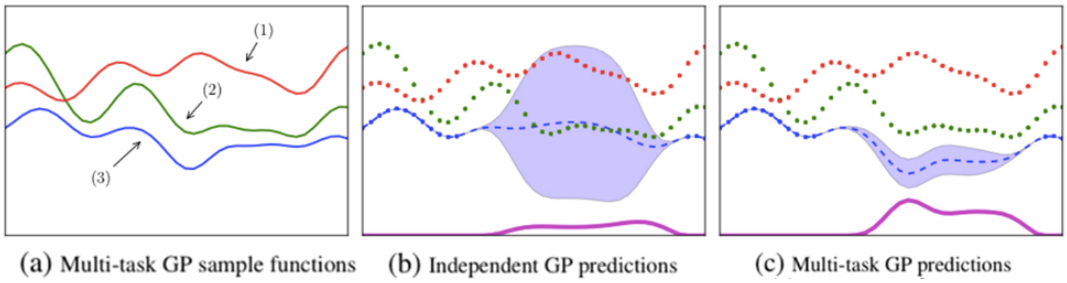

Figure 2.5: The Effect of Correlated Function on Gaussian Process Uncertainity [8]

2.4.1.3 Correlation of Methods

In order to use multi-fidelity approach, two solutions of numerical method should have a correlation. The Pearson correlation is used to measure how strongly two numerical methods are related [63]. Following formulation shows the calculation of Pearlson Correlation coefficient. Being close to 1 for Pearson coefficient means that there is a strong correlation.

$$r = \frac{\sum (x_i - \bar{x})(y_i - \bar{y})}{\sqrt{(\sum (x_i - \bar{x})^2 \sum (y_i - \bar{y})^2}} \tag{2.27}$$

where n_i denotes the sample values and $\bar{n}$ denotes the mean values

2.4.1.4 Acquisition Function

Acquisition function proposes the sampling points for Bayesian optimization. Prediction includes scores and uncertainty to give direction. There are many types of acquisition function to apply Bayesian optimization. Expected improvement (EI) is a widely used technique and based on exploration and exploitation.

Expected improvement is defined as

$$EI(x) = \begin{Bmatrix} (\mu(x) - f(x^+) - \xi)\Phi(Z) + \sigma(x)\phi(Z) & if & \sigma(x) > 0 \\ 0 & if & \sigma(x) = 0 \end{Bmatrix} \tag{2.28}$$

where

$$Z = \begin{Bmatrix} (\mu(x) - f(x^+) - \xi)/\sigma(x) & if & \sigma(x) > 0 \\ 0 & if & \sigma(x) = 0 \end{Bmatrix}$$

where $\mu(x)$ denotes mean and $\sigma(x)$ denotes the standard deviation of GPs posterior.

2.4.2 Sampling Method

Sampling is a process of distributing the set of variables in their limits. It's crucial the way of how widely the population is sampled because choosing a sample of individuals determines the searching outputs. Testing entirely the population is not feasible due to lack of resources and time so a considerable amount of studies use different techniques of sampling methods. Simple random sampling [64] is a prominent and widely used sampling technique because of easy implementation and availability in free software. A pseudo-random number generator is an example of simple sampling methods but they use specific mathematical expressions to arrange the irregularity of a distribution of individuals. The number of initial sets is determined by the dimensions of input space [65].

2.4.2.1 Sobol Sampling

Sobol sampling is a low-discrepancy quasi-random sequence. It is a productive method for higher dimension optimization problems. Distribution of points on initial state defines the behaviour of searching algorithms. When points condensed on a specific area, the surface model could not be well resolved for surrogate based optimization. Let $x_1, x_2, ..0 < x_i < 1$ to be generated as a set of numbers with low discrepancy in a given interval [66],[67].

$$x_n = b_1\nu_1 \oplus b_2\nu_2 + ... \tag{2.29}$$

where b_n denotes the binary representation of n and v_i is the direction numbers which represent a binary fraction.

2.4.2.2 Cross Validation

Cross validation is a validation of a model in machine learning techniques by subtracting limited data to be compared. Surrogate models are tested by comparing unavailable data in the domain. Cross validation uses train data to estimate the error of a given surrogate model [68]. Also, cross validation creates surrogate model by using converged hyper-parameters of a given surrogate model.

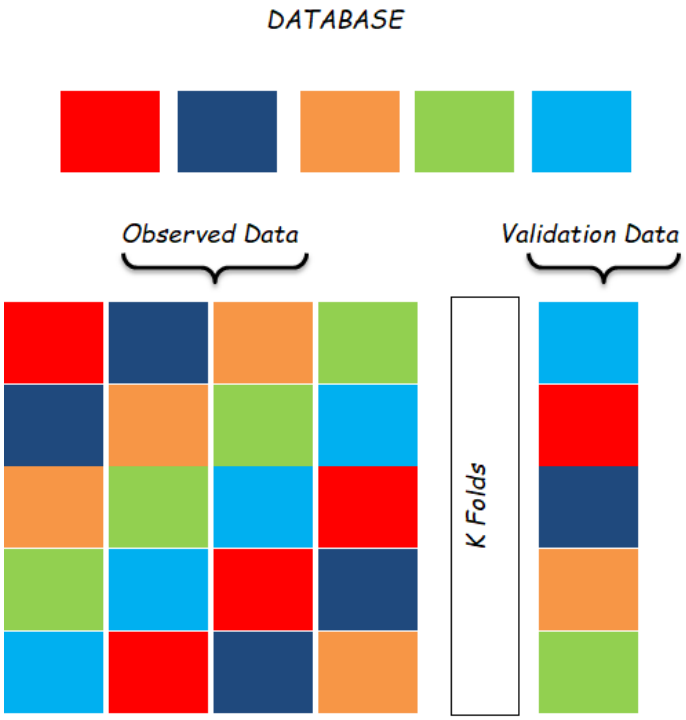

Figure 2.6: Schema of Leave One Out Cross-Validation

Figure 2.6 shows the schema of Leave-one out cross-validation. Parameter of k is a single indicator of the number that is taken out of the groups to be tested. Implementing these applications is known as k-fold cross-validation. Leave one out cross validation excludes each point building models at every single close out to estimate missing data.

2.5 Design Objectives

The objective function is a kind of mathematical expression or equation that represents the target that is to be optimized. There are basically two types of objective function in terms of formulation such as single objective and multi objective. Objective function is the main factor affecting directives of optimization algorithms since it defines the physics of a problem. When the system has many parameters, the weighted sum approach gives scale to each element of the objective function into a single value by giving a specific ratio and summation of each weight equals to one. Importance of the parameters in the objective function depends on the context or physics of the problems. In this thesis, there are three parameters that define the objective function. Equally important weights are given to normalized values of distortion coefficient, pressure recovery and mass of an intake.

Objective function,given as below, is defined as the weighted sum of normalize value of performance parameters

$$obj(x) = \sum_{i=1}^{n} \omega_i \left(\frac{\phi_i - \phi_{min}}{\phi_{max} - \phi_{min}} \right) \tag{2.30}$$

where ω_i denotes weights, n denotes the number of objectives and ϕ is the values of the objective parameter.

$$\begin{gathered} \sum_{i=1}^{3} \omega_i = 1 \\ w_{i-1} = w_i = w_{i+1} \end{gathered} \tag{2.31}$$

The reason for normalization is that there are difference in the order of magnitude for performance parameters.

2.5.1 Distortion Coefficient

Distortion coefficient is a non-dimensional parameter that defines the upcoming flow homogeneity. Aerodynamic interface plane (AIP) is a surface of the engine's compressor front-side. Flow inhomogeneity can lead to stall compressor blades and even

more beyond these, engine failure occurs. In order to avoid these detrimental effects on the compressor blade, intake geometry should be well designed.

$$DC\theta = \frac{\overline{P_{tAIP}} - \overline{P_\theta}}{Q_{AIP}} \tag{2.32}$$

where Q_{AIP} denotes the dynamic pressure at interfacing plane.

When the flow passes through the S-shape intake, secondary flow can occur. Detachment point for flow depends on the geometry of S-shape.

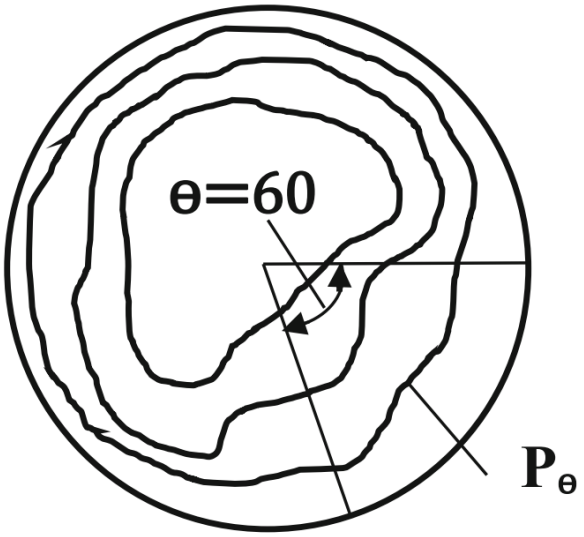

Figure 2.7: θ degrees slices of AIP for Distortion Coefficient [9]

Figure 2.7 shows the portion of θ angle sector for distortion coefficient.

2.5.2 Pressure Recovery

Pressure recovery is a ratio of total pressure values at engine face divided by free-stream total pressure. Flow strength is highly correlated with total pressure values. Geometry of S-shape is a main factor affecting losses in flow strength due to secondary flows.

$$PR = \frac{Pt_{AIP}}{Pt_\infty} \tag{2.33}$$

Desired values of PR is equal to one and it means there is no loss. Total pressure values include static pressure and velocity. Total pressure calculation is different because of the compressibility of flow. For incompressible flow, density is constant so that Bernoulli equation defines the total pressure. When density is not constant, isentropic relation is used to calculate total pressure under the assumption of calorically perfect air.

Instrumentation of total pressure is done with a number of across pressure probes located at air intakes. From each probe, readings are used for area weighted average of total pressure values.

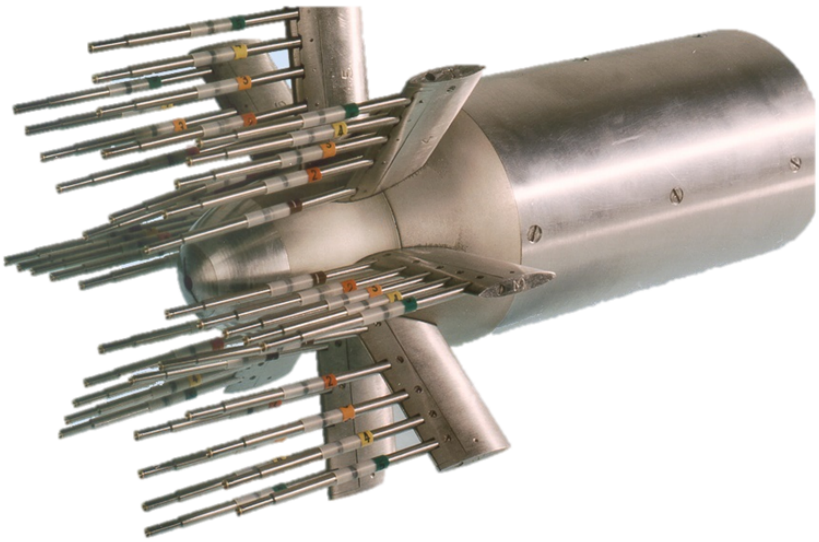

Figure 2.8: Air Inlet Pressure Rake ONERA [10]

Application to check whether pressure transducer reads real values or not is defined as calibration. There are some techniques of calibration under reference standard. Measuring error comes from instrumentation manufacturing, order of scale and outside effects.

2.5.3 Weight Estimation of a S-duct

Minimization of weight is an objective parameters as a stopping criteria in this thesis. While arranging flow performance of the intake, weight should be taken into account. Weight of a S-duct depends on volume size and material properties. In this study, it is assumed that same material is chosen for S-duct. Then, volume size of a S-duct is a single parameter for the weight calculation. Geometry of a S-duct is similar to a hollow circular cylinder. Figure 2.10 provides dimensions of a hollow circular cylinder.

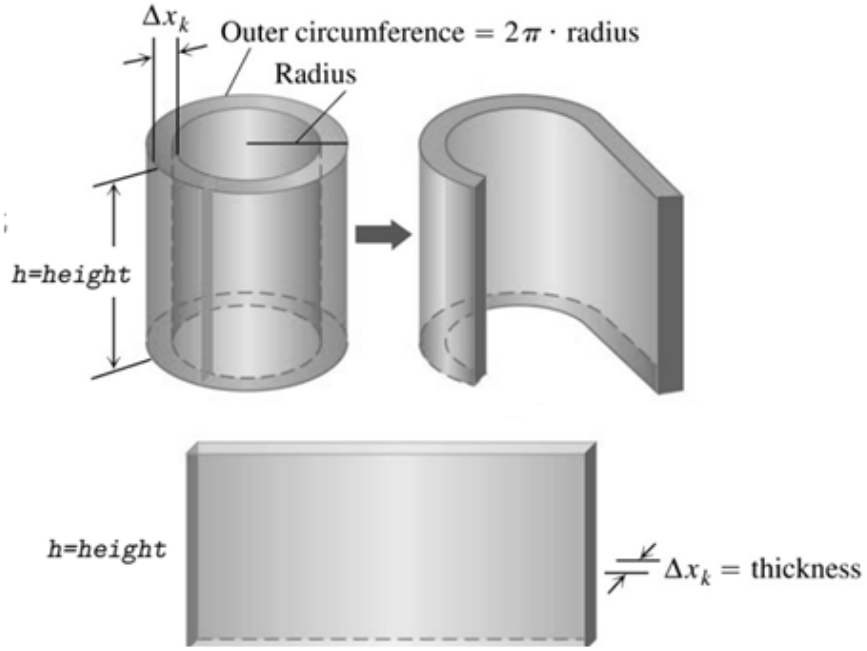

Figure 2.9: Volume by Cylindrical Shell [11]

The volume of a hollow circular cylinder is found by multiplying the circumference of the circular base times the height of the cylinder and thickness.

$$\begin{aligned} V &= A_{Perimeter} \times \Delta x_k \\ V &= 2\pi r \times h \times \Delta x_k \end{aligned} \tag{2.34}$$

Small thickness assumption simplifies the calculation of a shell volume.

$$V = A_{Perimeter} \quad when \quad \Delta x_k \approx 0 \tag{2.35}$$

where V denotes the volume and A is the surface area of a shell.

$$\Delta V_{S-duct} \sim \Delta A_{perimeter} \tag{2.36}$$

Normalized weight calculation of a S-duct is performed by using surface area values in the GAMBIT. Different surface areas for two intake model are given in Figure 2.10.

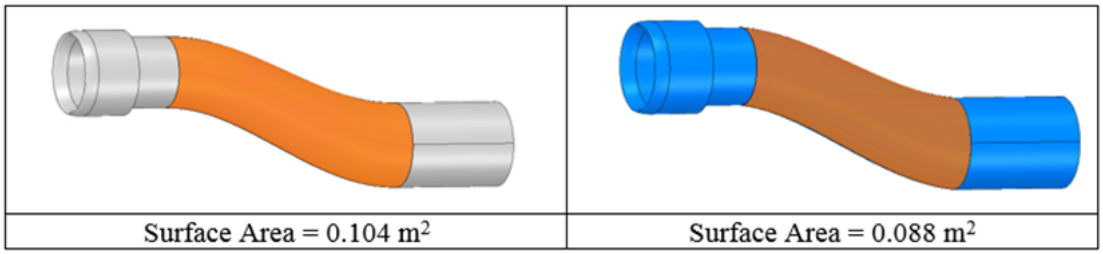

Figure 2.10: Different Surface Area Examples for S-duct

CHAPTER 3

VALIDATION STUDY FOR FLOW SOLUTIONS

In this chapter, a validation study for steady-state flow solutions to the RAE M-2129 subsonic intake is represented. This intake is one of the most commonly used subsonic intake models for numerical applications [16],[69].

First, the geometry of the RAE M-2129 intake is described. Then, the boundary conditions, and grid generation process are discussed, which is followed by a grid convergence study. As aforementioned all flow computations in this thesis are done using the commercial solver ANSYS Fluent ©. The numerical models available in this solver are explored for steady flow solutions. Different cost levels of analysis method are necessary in multi-task Bayesian optimization, and therefore a turbulence model selection study is carried out first. Validation is carried out comparing the static pressure values yielded by different turbulence models across the entire duct's upper and lower sides. Pressure recovery, distortion coefficient, Mach number, and static pressure ratio at AIP plane are also investigated comparing with the available wind tunnel measurements [12].

3.1 RAE M-2129 Subsonic Diffuser

M-2129 S-diffuser geometry was designed by QinetiQ and supplied to AD/AG-43 Groups to perform numerical analysis for comparisons. The model has a formulated circular cross-section whose center is aligned on the line of S-shaped.

$$D = D_{throat} + (D_{AIP} + D_{throat}) \left[3 \left(1 - \frac{x}{L} \right)^4 - 4 \left(1 - \frac{x}{L} \right)^3 + 1 \right] \tag{3.1}$$

S-shaped is formulated as follows,

$$y = -0.15\left[1 - cos(\frac{\pi x}{L})\right] \tag{3.2}$$

Table 3.1: Geometric Parameters of RAE M-2129

Parameters	Symbol	Values [mm]
AIP Location	x_{AIP}	483.9
Duct Lenght	L	457.2
Entry Diameter	D_c	144.0
AIP Diameter	D_{AIP}	152.4
Throat Diameter	D_{throat}	128.8

The parameters in Equation 3.1 and 3.2 are tabulated in Table 3.1

The diffuser has an inlet-lip, then an S-duct and a straight channel after AIP. Coordinate representation of the diffuser at side view is illustrated in Figure 3.1.

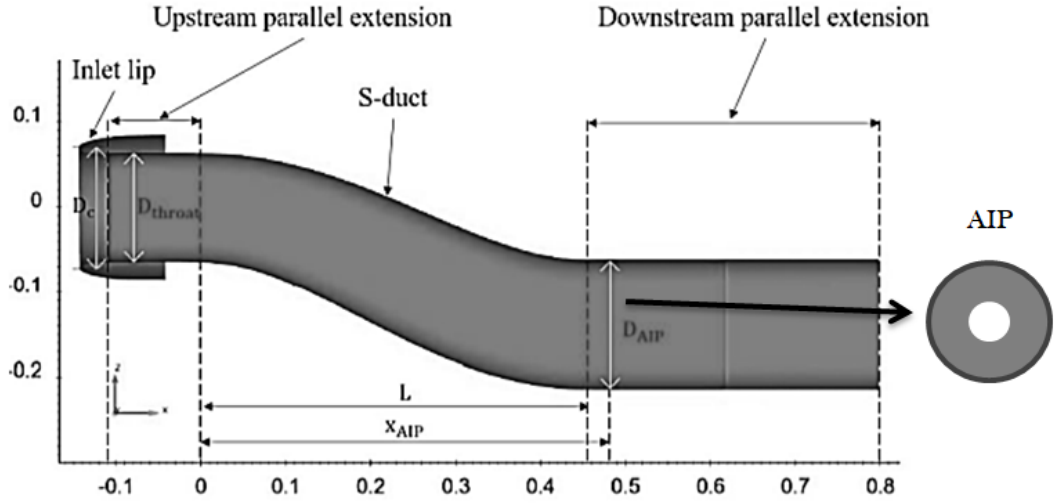

Figure 3.1: Side-view Geometrical Represantation of RAE M-2129 [12]

3.1.1 Solid Model Detail

The Computer aided graph version of the model is drawn with given formulated data in GAMBIT software. Figure 3.2 shows isometric views of RAE M-2129 CAD Model.

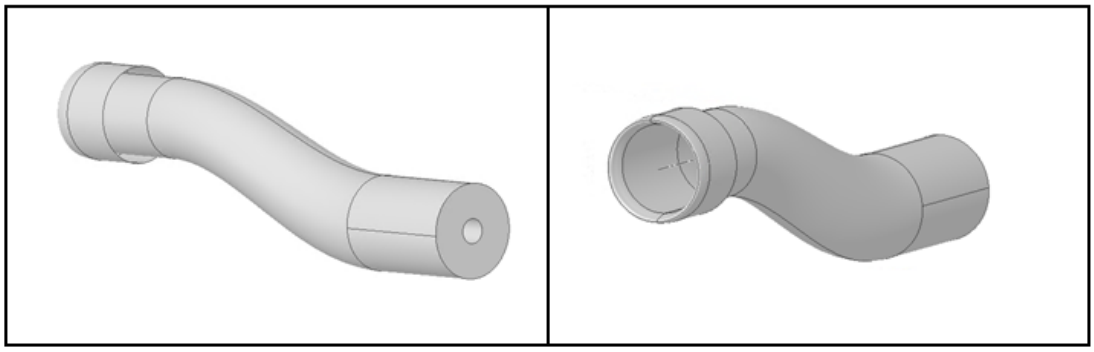

Figure 3.2: CAD Model of RAE M-2129

The straight duct segment at the lip is the first component which interacts with the upcoming free-stream flow.

3.1.2 Boundary Conditions

Numerical solvers use boundary conditions to simulate the real condition. Far field is created at the outer surface of the control volume to imply free-stream conditions with specified Mach number, constant pressure and temperature values. An adiabatic and no-slip wall boundary condition are used to represent the intake surfaces. The back-end surface of S-shape is set as a pressure outlet boundary condition to simulate the effect of an engine.

Boundary conditions for the test case are illustrated in Figure 3.3.

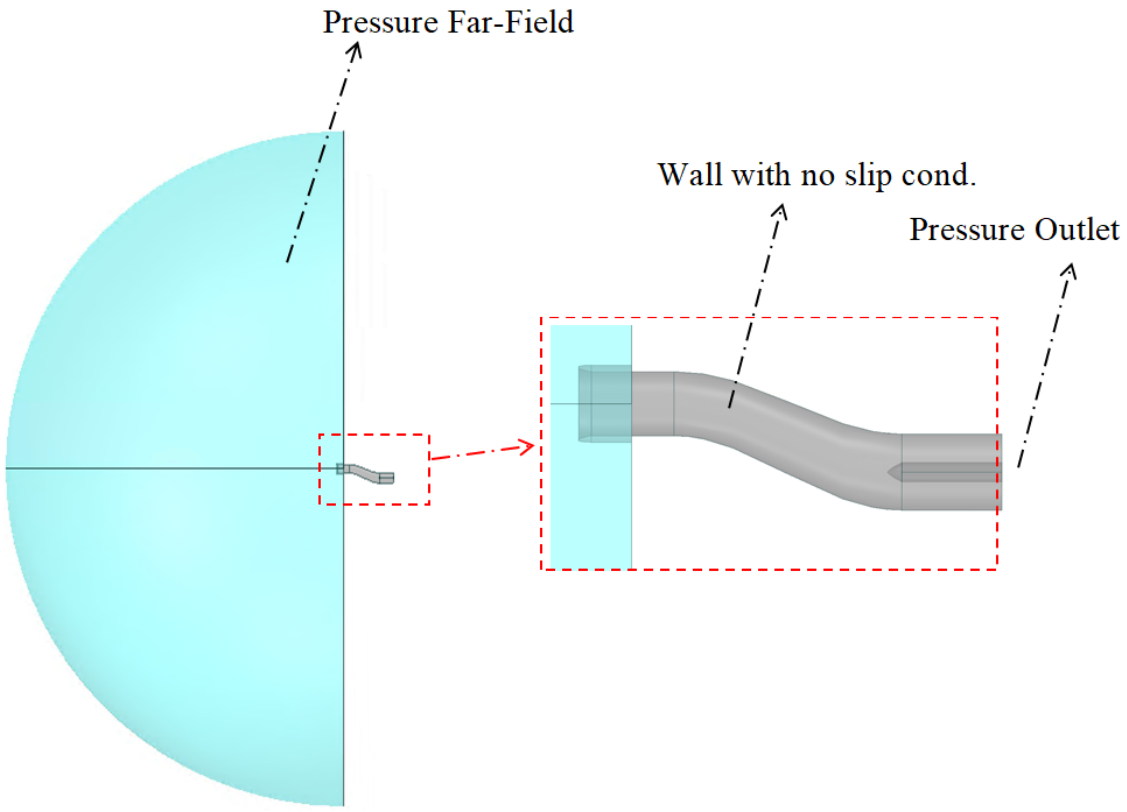

Figure 3.3: Boundary Conditions of RAE M-2129 Test Case

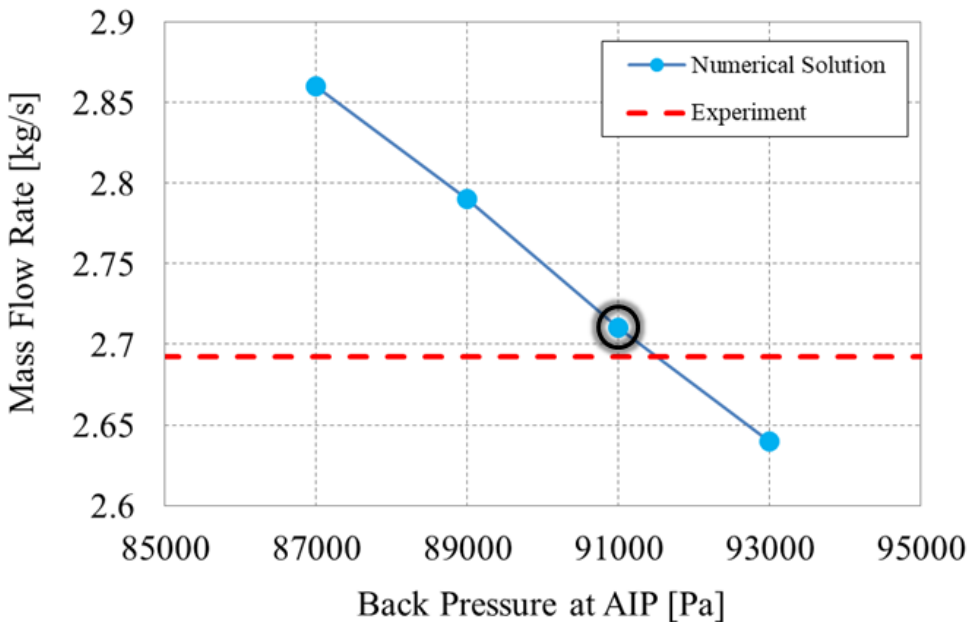

Figure 3.4: Mass Flow Rate with respect to Back Pressure at AIP

From the test condition of RAE M-2129, pressure values are iteratively set to cap-

ture mass flow rate at AIP in Figure 3.4, and Mach number, pressure recovery and distortion coefficient are all monitored during the iterative solution.

Far-field and outlet boundary condition is given in Table 3.2

Table 3.2: Flow and Boundary Conditions[2]

Parameters	Values
Mach Number (M_∞)	0.204
Total Pressure (P_{t_∞})	105139.5 Pa
Total Temperature (T_{t_∞})	293.7 K
Angle of Attack (α)	0^0
Sideslip Angle (β)	0^0
Mass Flow Rate ($\dot{m}$)	2.692

3.1.3 Grid Generation

When it comes to engineering simulation of a field with discretization, meshing plays a crucial role. One of the most important considerations for ensuring numerical accuracy is the creation of a high-quality mesh. In other words, face and cell elements of mesh should have a good quality for stable numerical analysis. Skewness is a primary indicator of quality. It is an angle measuring technique related with equilateral triangle/quadrangle.

To capture turbulence, y^+ values which is a non-dimensional first cell distance to the wall should be close to 1 for the selected numerical models in this thesis. The formulation of y^+ is given below,

$$y^+ = \frac{u_* y}{\nu} \tag{3.3}$$

where u_* denotes friction velocity at wall and ν denotes the kinematic viscosity of the fluid.

In the validation analysis, the first cell height in the boundary layer is calculated as 5×10^{-3} mm for the given test condition. Total number of elements in the boundary layer is taken as about 25 with a stretching ratio of 1.15 outward. The constructed

grid has skewness values of under 0.8 for the surface and 0.95 for the cells.

Flow regions with shocks, shear layer interactions and expansion waves involve high gradients and should be discretized with high resolution. However, denser mesh elements cause to quite extensive calculations, and therefore an optimum number of elements should be determined for reasonable cost.

The details of volume mesh and boundary layer grid in the duct are illustrated in Figure 3.5.

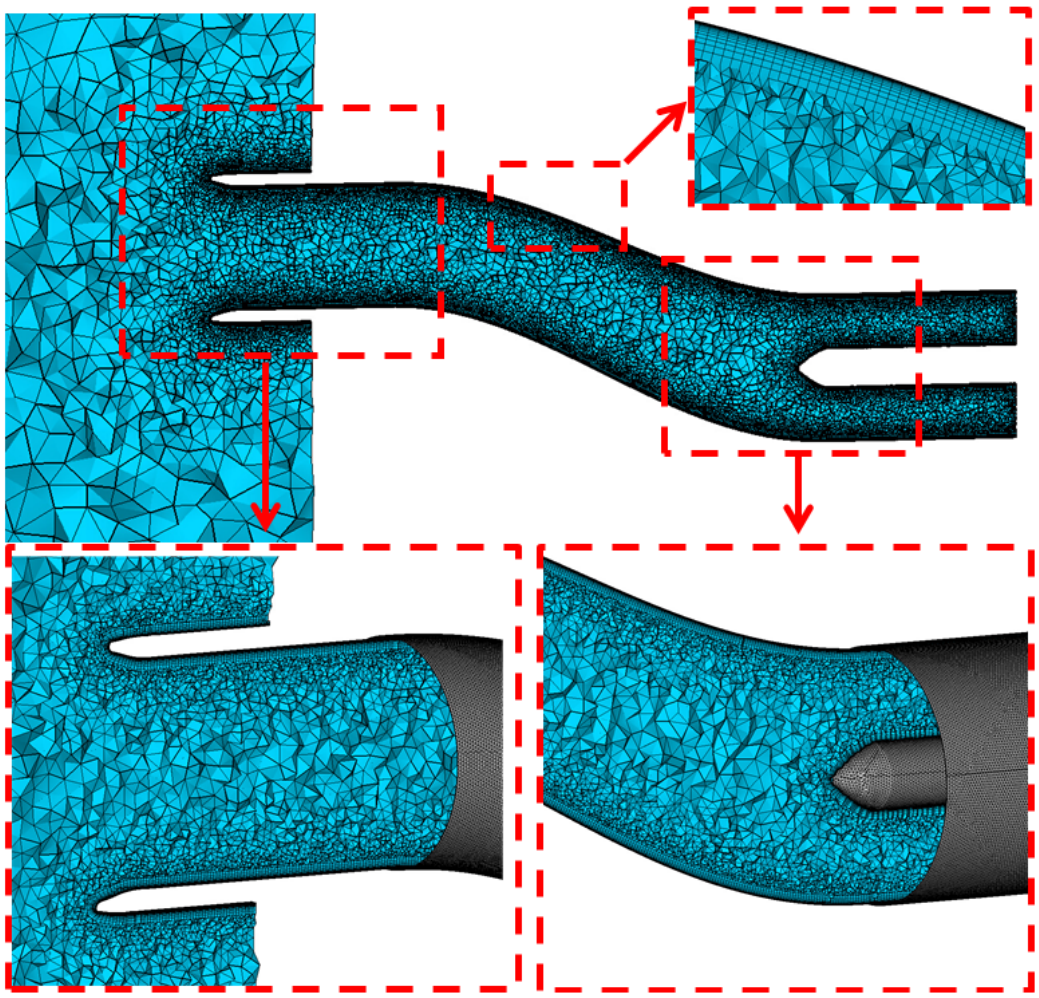

Figure 3.5: Numerical Elements of RAE M-2129 Test Case

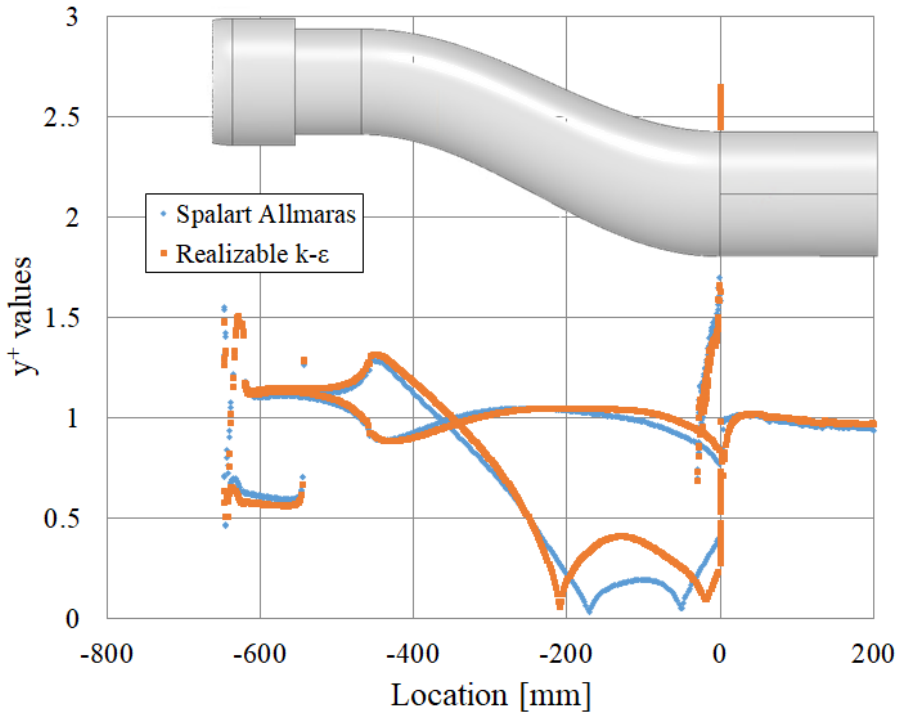

Figure 3.6: y^+ values over RAE M-2129 Walls

y^+ values for two different cost of numerical models is plotted in Figure 3.6

3.1.4 Solvers Setup

ANSYS Fluent © offers two different numerical methods which are pressure based and density based. Although pressure based solvers are used for low-speed flow and density based solvers are used for high-speed flow, the two methods have been modified to expand for a wide range of flow conditions . In the density-based algorithm, the pressure field is obtained from the equation of state. The continuity equation is used for the density field [55]. For pressure based solver, continuity and momentum equations are manipulated to be formed as a pressure-correction equation. Pressure fields are obtained from pressure-correction equations.

The solvers used in multi-tasking optimization of the present work are coupled, pressure based 3-D RANS with the Spalart-Allmaras (S-A) turbulence model for low-cost results, and density based 3-D RANS with the realizable k-ϵ turbulence model for the high-cost result.

To achieve convergence for steady state analyses, permissible CFL numbers are selected. When the smooth convergences are achieved, total iteration numbers are 3500 for low-cost method and 6500 for high-cost method.

3.1.5 Grid Convergence Study

The independence grid study is used to ensure that the solutions are not affected by the grid size. To eliminate the errors in the solution due to the insufficient number of grid size, grid independence study is carried out until the solution does not change for each turbulence model. The grid convergence study for RAE M-2129 is performed with a sequence of coarse ($\sim$5 million cells), medium ($\sim$10 million cells), and fine ($\sim$20 million cells) meshes. Figure 3.7- 3.8 show the details of the mesh near AIP.

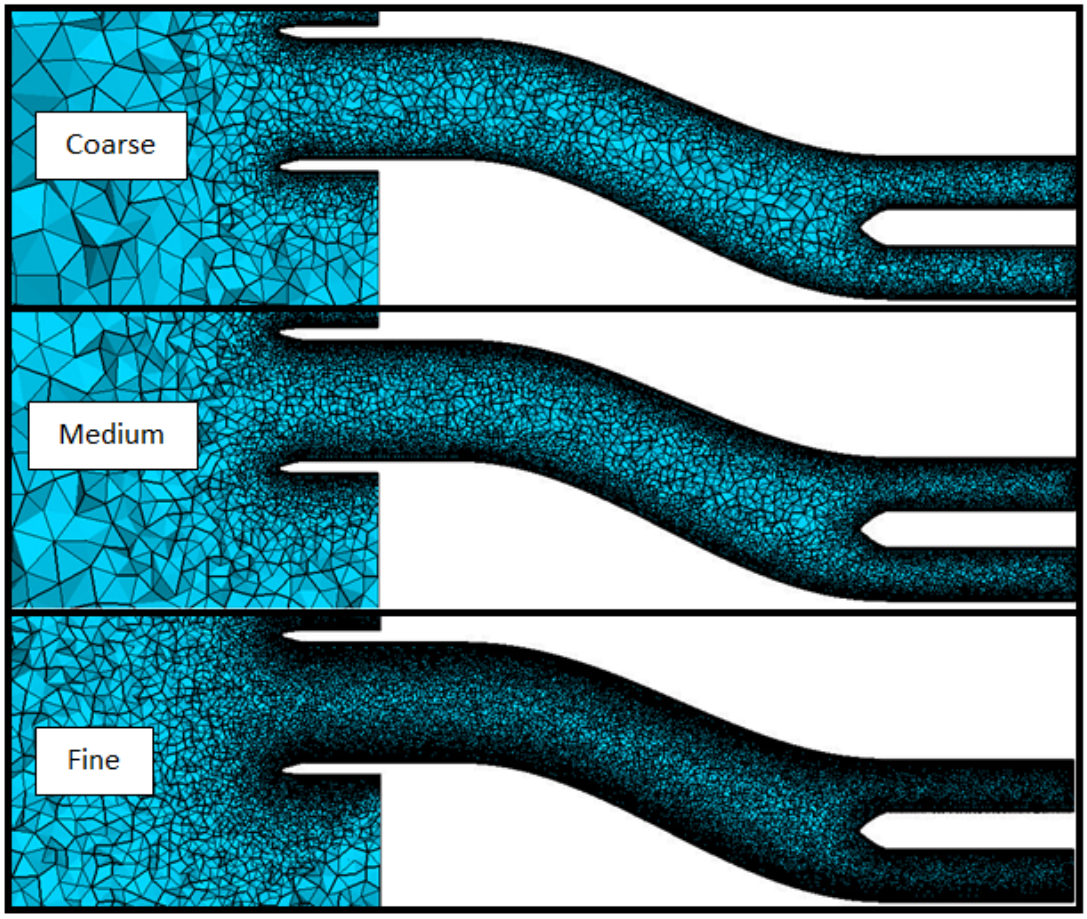

Figure 3.7: Grid Convergence Study of RAE M-2129

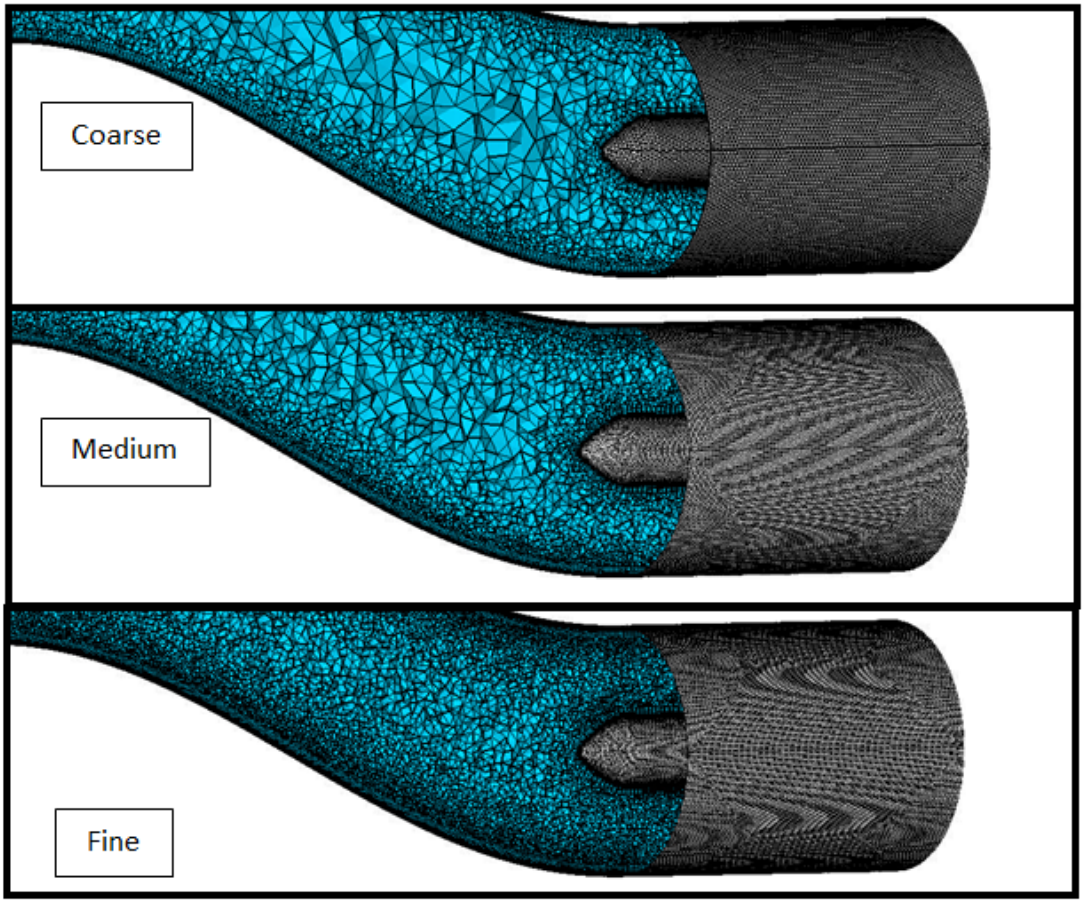

Figure 3.8: Grid Convergence Study of RAE M-2129 Engine Inlet

Grid sensitivity study is carried out for each numerical solver, and the distortion coefficient and pressure recovery values at AIP are determined with respect to the number of elements. It is obtained that the values of pressure recovery and distortion coefficient do not change and the differences are less than 1 % when the element size is equal to or higher than the medium size in Figure 3.9 and 3.10.

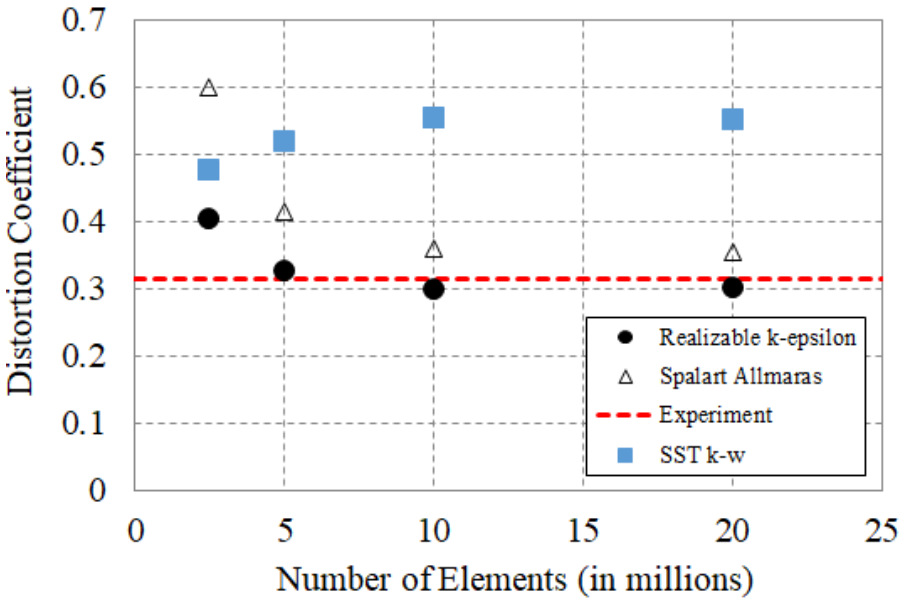

Figure 3.9: Distortion Coefficient for Different Element Size

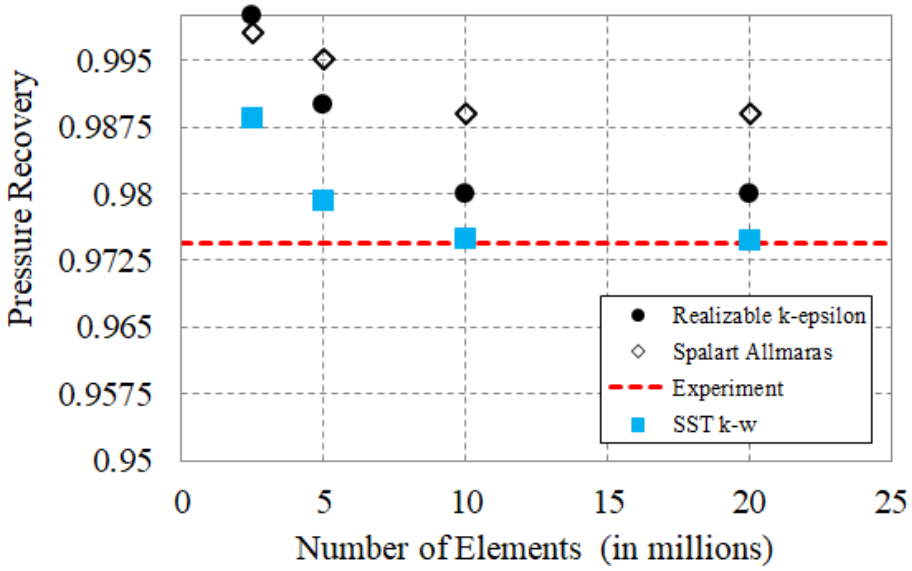

Figure 3.10: Pressure Recovery for Different Element Size

3.1.6 Turbulence Models Selection According to Cost Levels

Validation of RAE M-2129 model is performed to simulate real physics. Cost of numerical model is defined that it is a trade-off between computational effort of the turbulence model and level of error in the solution. For high and low cost turbulence model selection, realizable k- ϵ, SST k-ω and Spalart-Allmaras are used for multi-task Bayesian Optimization [69],[17],[16]. After setting the boundary conditions with a suitable mesh model, the flow Mach number, pressure recovery, mass flow rate, and static pressure ratio values are monitored during the iterations

Experimental data are taken from the technical report of the GARTEUR AD/AG-43 [2], "Application of CFD to High Offset Intake Diffusers". Performance outputs at interfacing face for the bullet model named DP78 are tabulated in Table 3.2

Table 3.3: DP78 Experimental Data[2] of RAE M-2129 with bullet

Parameters	Values
AIP Mach Number	0.419
$\dot{m}$ (kg/s)	2.69
Pressure Recovery	0.9744
PRA	0.8522
DC60	0.313

In table 3.3, static pressure ratio (PRA) is the area-weighted average static pressure values over ambient total pressure.

The flow results of the turbulence models at the interfacing plane are compared to experimental data in Table 3.4.

Table 3.4: Comparisons of Flow Variables at AIP for Turbulence Models and Experimental Data (DP78)[2]

Turb. Methods	Back Pressure	Mach Number	$\dot{m}$	DC60	PR	PRA
Experiment	-	0.419	2.69	0.313	0.974	0.85
Realizable k-ϵ	91000	0.422	2.71	0.297	0.981	0.86
SST k-ω	88000	0.394	2.68	0.551	0.975	0.84
Spalart-Allmaras	91000	0.389	2.65	0.362	0.952	0.87
k-kl EARSM [2]	91800	0.381	2.63	0.464	0.984	0.87

The difference between experimental data and numerical results are calculated. Mach number at AIP is calculated with area-weighted average values. With increased mass flow rate, the Mach number at the interfacing plane rises. Other turbulence models, in particular, have failed to estimate the distortion coefficient. Each turbulence model finds pressure recovery values close to the experimental results and errors in the calculated mass flow rate values are less than 1 % at AIP. For this reason, the distortion coefficient (DC60) is the determining parameter in the selection of the turbulence model according to the cost level. DC60 obtained from realizable k-ϵ turbulence model is closer to experimental data. The solution time for the realizable k- ϵ turbulence model is about 3 hours on 240 CPU Processors. Realizable k- ϵ is selected as a high cost turbulence model for multi-task Bayesian optimization due to low error in DC60 and execution time of an analysis.

Spalart-Allmaras turbulence model is selected as a low cost numerical method for multi-tasking Bayesian optimization. Compared to the experiment, the Spalart-Allmaras has a 15% error value in the DC60 value. Also, solution time for is obtained nearly 1 hour with 240 number of CPU Processors.

Following figure shows the comparisons of total pressure contours for CFD applications and experiment.

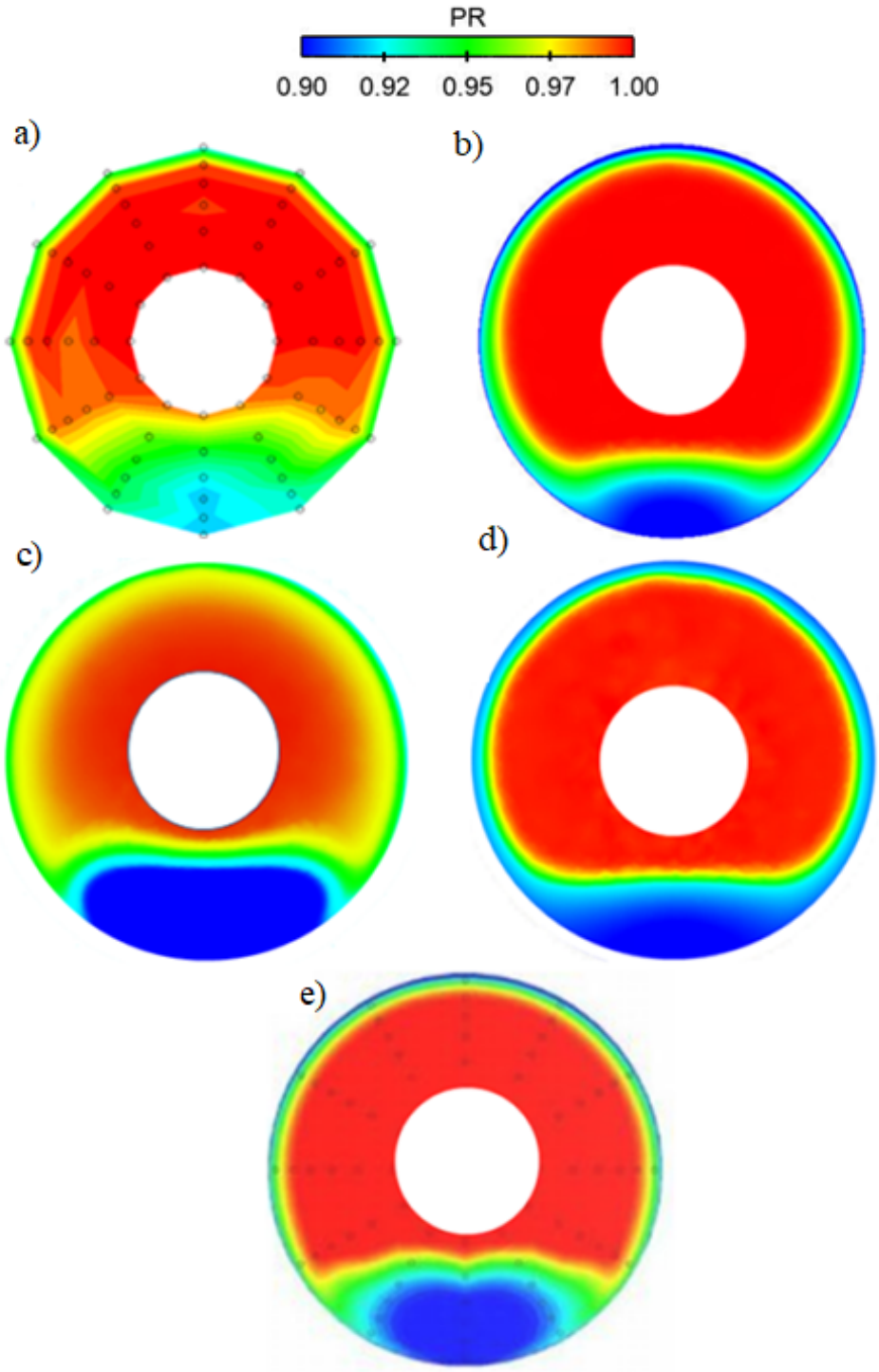

Figure 3.11: Comparisons of Pressure Recovery Contours for RAE M-2129 (a) Experimental Measurement DP78 [2], (b) Realizable k-ϵ Turbulence Model,(c) SST k-ω Turbulence Model , (d) Spalart Allmaras and (e) k-kl EARSM Turbulence Model [2]

Analysis results in Figure 3.11 show the losses on the flow quality. The difference on the distribution on pressure recovery comes from the secondary flow modelling. The k-ϵ turbulence model predicts pressure recovery trends that are similar to those observed in the experiments. The small total pressure values near wall are obtained due to effects of skin friction. Also, separated flow region at the bottom of AIP is captured to certain extent by Spalart-Allmaras.

The static pressure ratios of the walls are compared at the upper and bottom of the inlet section across the duct in Figure 3.12

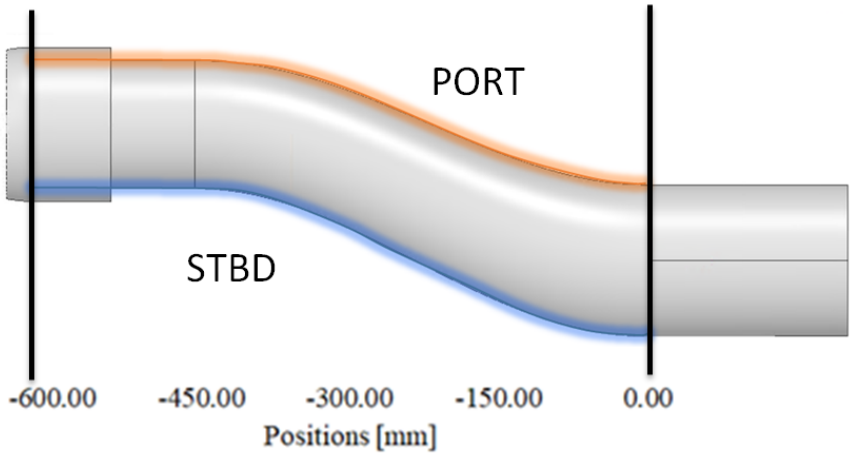

Figure 3.12: Upper and Bottom of the Inlet Section Across the Duct

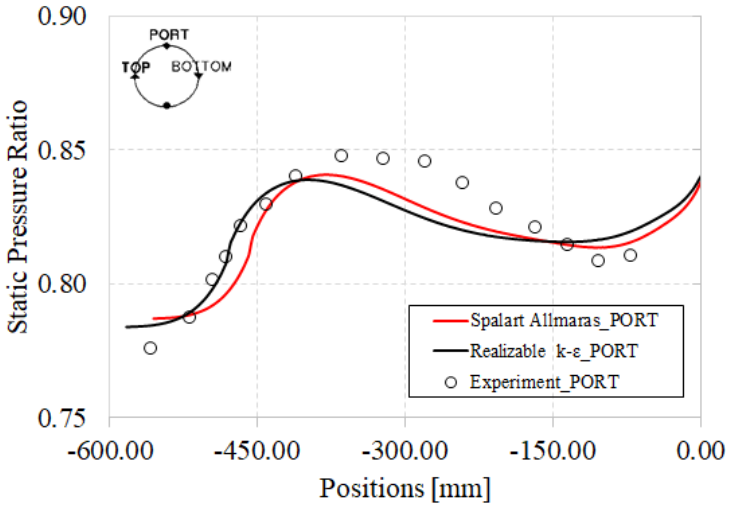

Figure 3.13: Comparison of Wall Static Pressure Ratio for Experimental Measurements and k-ϵ Turbulence Model at PORT[2]

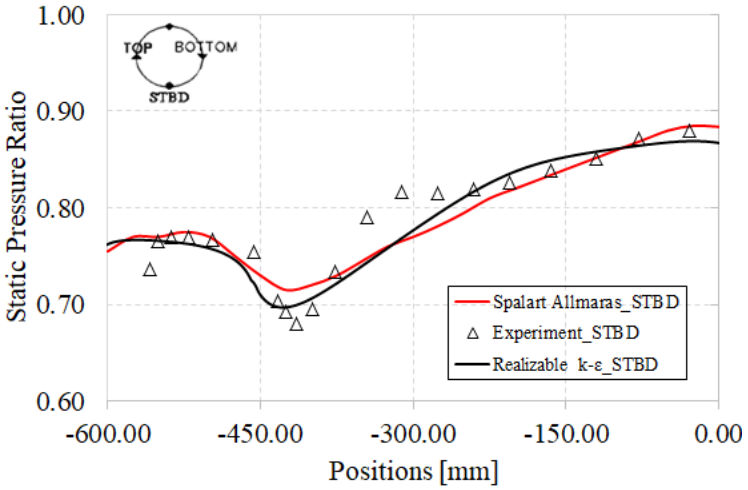

Figure 3.14: Comparison of Wall Static Pressure Ratio for Experimental Measurements and k-ϵ Turbulence Model at STBD[2]

The static pressure ratio at AIP is higher at the bottom section due to secondary flow. Also, separation starts at x = -450 mm shown in Figure 3.14. Static pressure ratios across the duct are well captured by realizable k-ϵ turbulence Model. Wall duct pressure ratio comparison in Figure 3.13 shows that low cost turbulence model and high cost turbulence model have similar predictions and they have a small differences in static pressure ratio at the upper section.

Contours of Mach number are compared for k-kl EARSM turbulence model [2], realizable k-ϵ Turbulence Model and Spalart- Allmaras. Figure 3.15 shows three different numerical analysis details about inner flow characteristic and separation zone at mid-section. It is easy to understand that separated flow affects the total pressure distribution at the interfacing plane. Low total pressure region differs slightly in turbulence models.

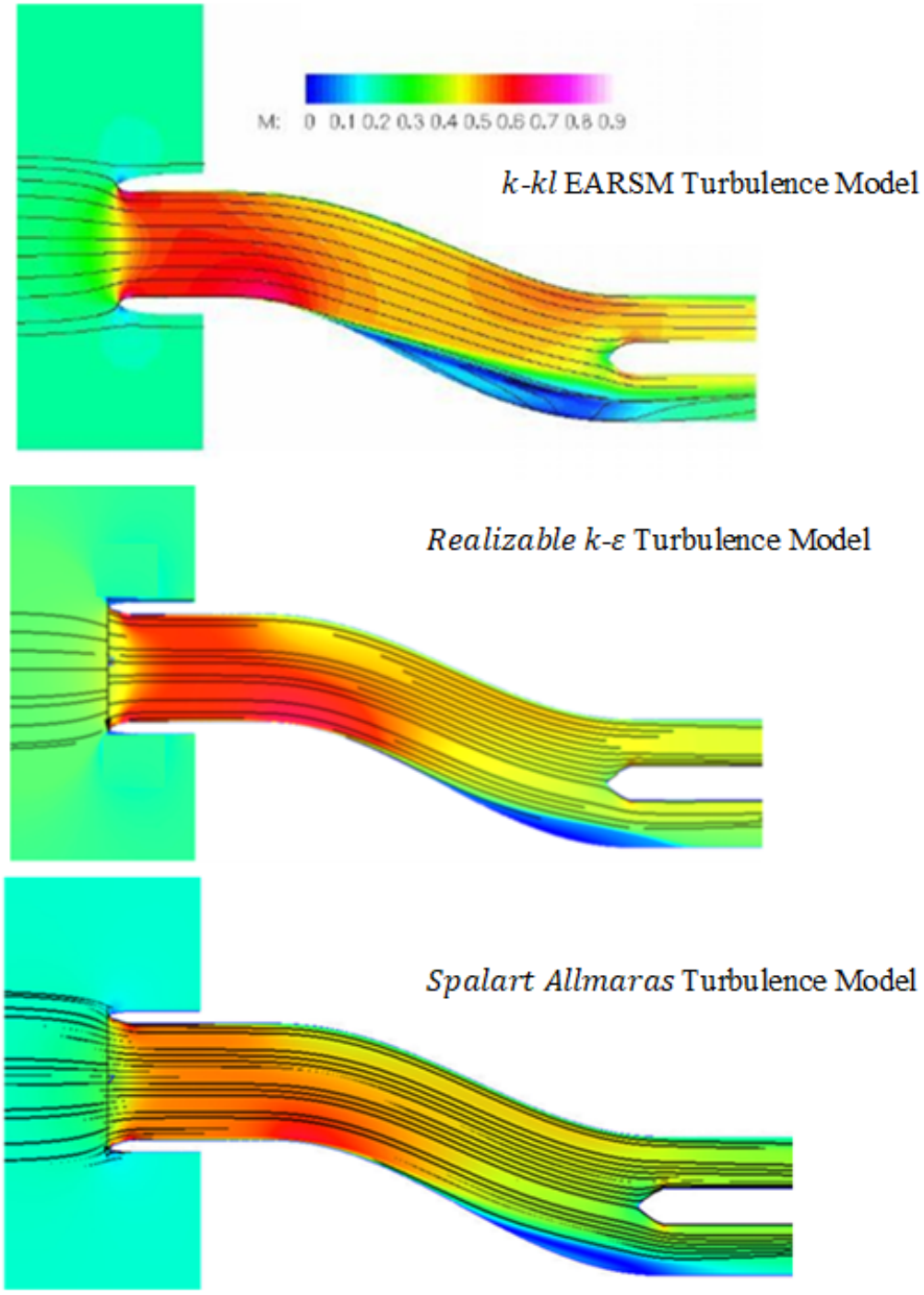

Figure 3.15: Comparison of Mach Contours for k-ϵ Turbulence Model, Reference Turbulence Model (k-kl EARSM) [2] and Spalart- Allmaras Turbulence Model at mid-section

CHAPTER 4

OPTIMIZATION RESULTS AND DISCUSSION

In this chapter, results of shape optimization by multi-task Bayesian application are explained and supported with detailed discussions. In the optimization study, baseline of intake is selected as RAE M-2129. Bezier control points that represent the RAE M-2129 geometry are required to be calculated. For this reason, y-coordinate difference of selected span-wise locations between Bezier representation and analytical formulation of RAE M-2129 iterated until satisfactory root mean square error value is obtained. The root mean square error definition is given in Equation 4.1.

$$RMSE = \sqrt{\frac{\sum_{i=1}^{N}(y_i - \hat{y})^2}{N}} \tag{4.1}$$

where N is the number of points, y_i denotes values from the Bezier curve and $\hat{y}$ denotes values from the analytical formulation.

Figure 4.1 shows matching Bezier representation of RAE M-2129 (black-dashed) with curve obtained from its analytical formulation(red-line).

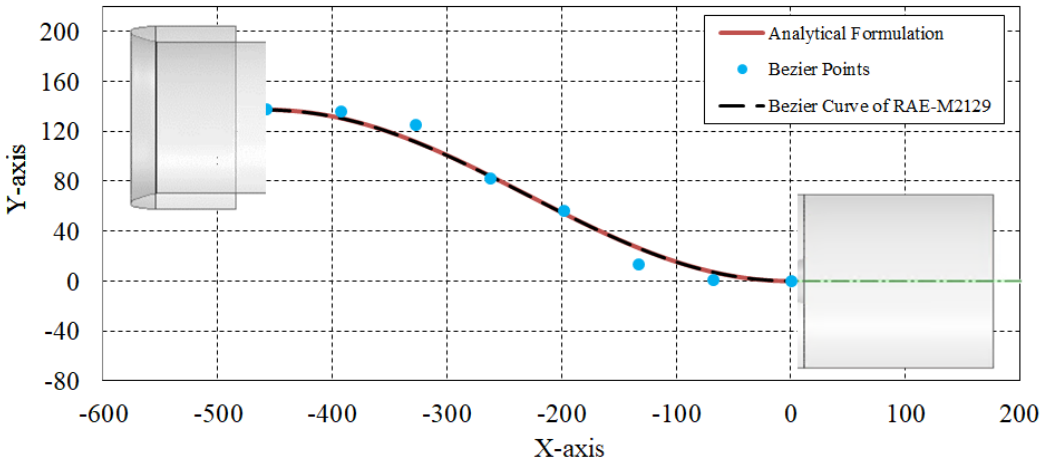

Figure 4.1: Bezier Representations of RAE M-2129 with Analytical based S-line

Bezier points that represent RAE M-2129 is given in Table 4.1. The upper and lower boundaries of Bezier parameters for optimization study is defined based on the Bezier parameters of the RAE M-2129. Additionally, the length of the duct is an another input parameter. Its boundary changes in $\pm$ 100 mm around the value in the baseline. The input baseline values, upper and lower boundaries are tabulated in Table4.1

Table 4.1: Boundaries of Inputs for Optimization

Parameters	Lower Bound	Baseline(RAE M-2129)	Upper Bound
y_1	146.00	136.00	121.00
y_2	140.00	125.00	110.00
y_3	97.00	82.00	67.00
y_4	71.00	56.00	41.00
y_5	28.00	13.00	-2.00
y_6	16.00	1.00	-9.00
ΔL	-100.00	0.00	100.00

Line continuity problem is observed for some design alternatives. The reason is resulted to be broad range of y_1 and y_6. In order to overcome line continuity problem, the range of y_1 and y_6 is reduced. Figure 4.3 shows an example of line continuity problem.

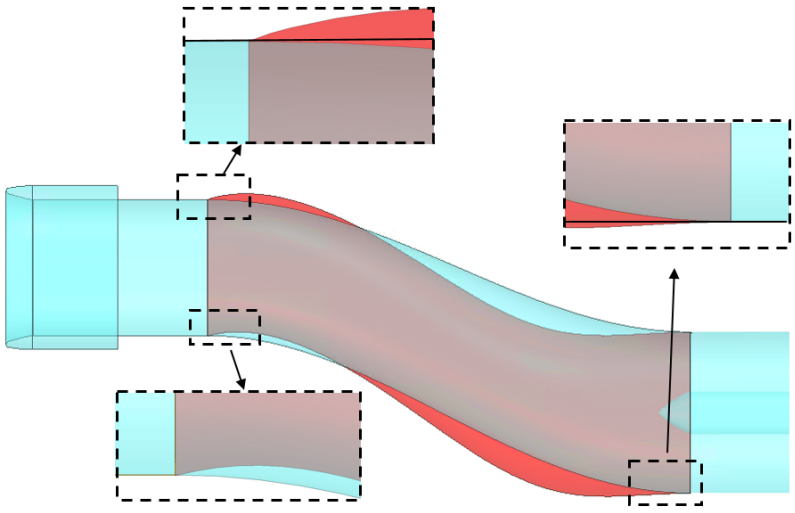

Figure 4.2: An Example for the Failure of Bezier based Model

As it is aforementioned in section 2.4.1.3, Bayesian application requires that analysis methods with different accuracy levels have a strong relationship. Pearlson correlation coefficient is calculated as 0.945 which is sufficient for multi-task Bayesian optimization. Moreover, Figure 4.3 shows the correlation of high and low cost models objective values. The objective function is a combination of normalized pressure recovery, distortion coefficient and duct weight. The correlation between two numerical models is evaluated as sufficient.

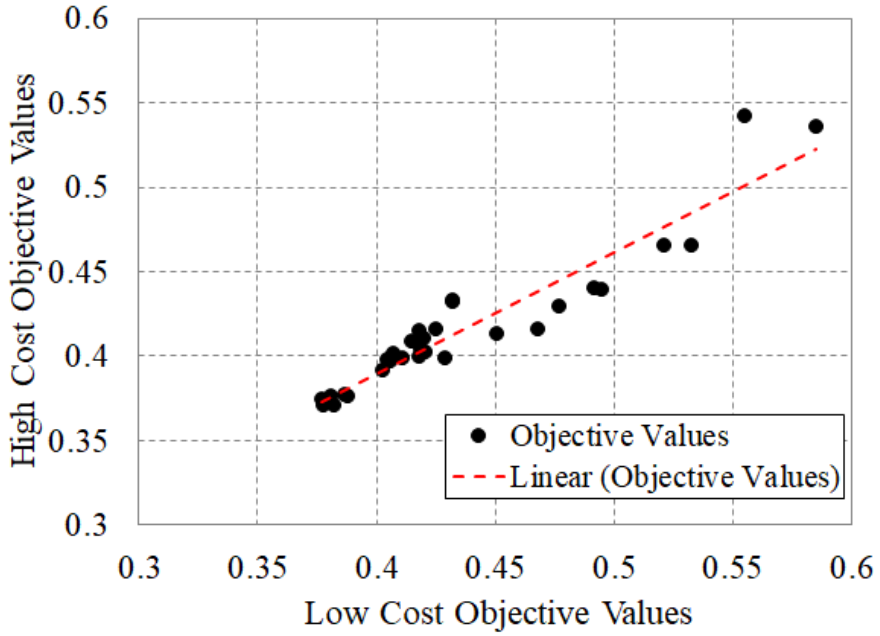

Figure 4.3: Comparison between High Cost Numerical Results and Low Cost Numerical Results of Intake Samples

The correlated models are used to test the prediction success of Gaussian process. The reason why these demonstrations are performed is to understand how well the Gaussian process can learn from the training data. A total of 30 arbitrarily selected design points are solved with two different cost levels of turbulence models. An open source data prediction tool for multi-task Bayesian application is employed in Gaussian process. Figure 4.4 shows the differences between objective values of low and high cost methods.

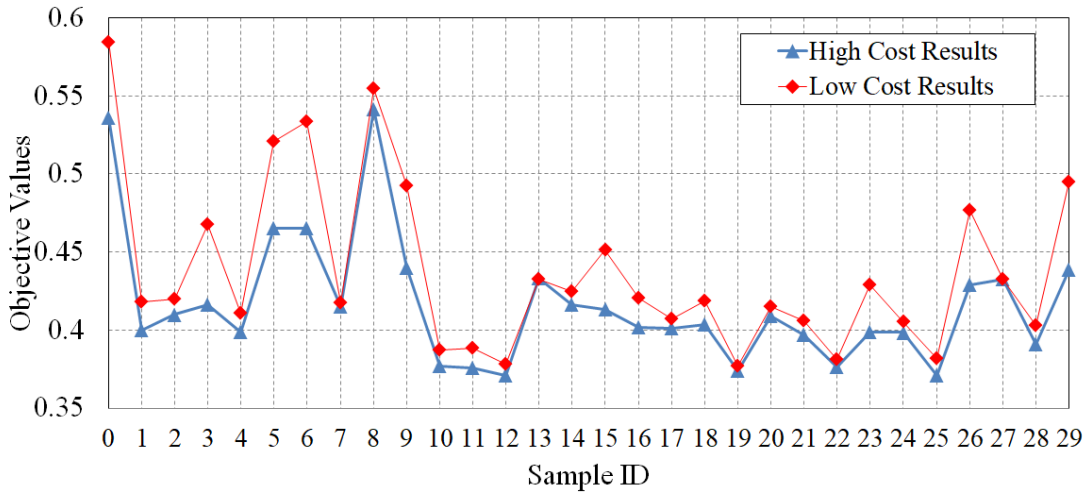

Figure 4.4: Objective Values of Two Different Cost Turbulence Models over Sample Numbers

In Figure 4.4 each sample which has specific inputs of $y_1, y_2, y_3, y_4, y_5, y_6$ and L values represents the S-duct configuration. Objective values from numerical solutions are used in the Gaussian process to model the distribution. Regression analysis is used to estimate 5 different samples in Table 4.2.

Table 4.2: Parameters Detail of a Gaussian Process Application of a given 5 Control Points (CPs)

ValuesID	CP-1	CP-2	CP-3	CP-4	CP-5
y1[mm]	137.2609	141.2418	139.3542	138.9812	140.0333
y2[mm]	132.1630	130.5458	130.4317	133.5354	133.9270
y3[mm]	73.6903	73.1234	77.1520	76.1348	74.5686
y4 [mm]	51.5888	51.8987	49.7011	53.1587	46.3715
y5[mm]	25.5671	24.2423	23.3283	23.9812	25.0329
y6[mm]	1.2430	1.4776	0.4341	0.3050	4.6238
L [mm]	9.865	31.832	38.971	13.810	19.038

The predicted values from the Gaussian process and high cost numerical results of these samples are compared to show the regression analysis achievement in Figure 4.5

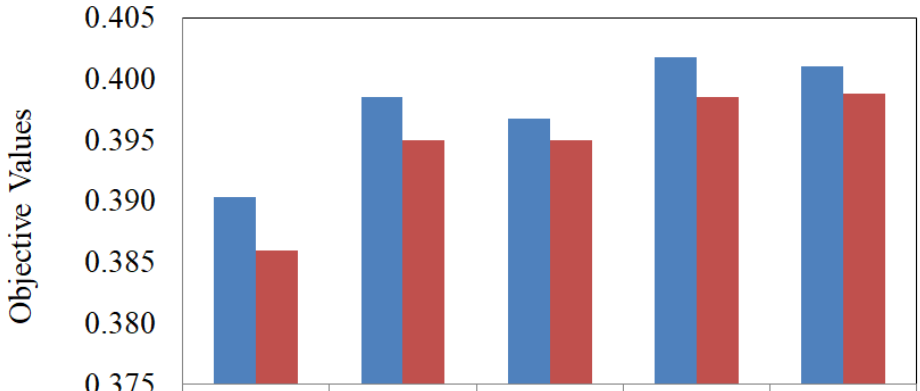

	Control Point-1	Control Point-2	Control Point-3	Control Point-4	Control Point-5
High Cost CFD	0.39034	0.39848	0.39677	0.40178	0.40106
Gaussian Prediction	0.38600	0.39500	0.39500	0.39850	0.39880

Figure 4.5: Comparison for High Cost CFD Results and Gaussian Prediction over Control Points

Demonstration of the Gaussian process shows valuable prediction over given samples test data. Each prediction error is less than 1%. It can be stated that prediction of Gaussian Process can be used as an high cost solution.

Optimization study is performed for different size of initial sampling and the performance comparison between multi-tasking and single tasking. Firstly, multi-task Bayesian optimizations are employed for the effect of initial sample size on optimization to compare the convergence speed. In order to check the surrogate model capability, leave one out cross-validation (LOOCV) is applied for each optimization with different number of sampling. Secondly, single tasking is performed to compare multi-tasking Bayesian optimization for execution time comparison.

Relation between performance parameters in the objective function are investigated with Pareto plots. In addition, related figures point out the outcomes. Lastly, contours comparison are drawn for the baseline and optima.

4.0.1 Effects of Initial Sampling Size on Optimization

Multi-Task Bayesian optimization starts with the initial set of sample to understand the system behaviour. All starting points are analysed with two numerical applications for Gaussian Process. Then, optimization continues with cycles which includes proposed design points by acquisition function. Low cost and high cost analysis are performed also in the optimization cycles. In this part, the effects of a number of initial points are investigated on convergence performance. Multi-task optimization parameters are given in Table 4.4.

Table 4.3: Input Settings of Multi-Task Bayesian Optimization Application

Parameters	Definition	Values
n-init-cfd-ke	Size of the quasirandom initialization HCOST RUN	5-10-20
n-init-cfd-sa	Size of the quasirandom initialization LCOST RUN	5-10-20
n-opt-cfd-ke	Batch size for BO selected points to be HCOST RUN	5
n-opt-cfd-sa	Batch size for BO selected points to be LCOST RUN	15

Optimization starts with high cost and low cost performance values of intake samples selected by Sobol sequence. Then, Bayesian optimization constructs a probabilistic model using Gaussian Process. Acquision function gives scores of the surrogate model to select the next sample from the search space. The selected 15 number of intake models (n-opt-cfd-sa) are analyzed with low-cost models in optimization cycles. Then, 5 intake models (n-opt-cfd-ke) out of these 15 intake models have higher fitness values between them. Then, high accuracy analysis is used for these 5 intake models to train the surrogate model. Updating surrogate model in each cycle is also referred as machine learning. This multi-task optimization is applied at each cycle until the convergence is achieved.

Figure 4.6 shows the mechanism of open source multi-tasking Bayesian optimization.

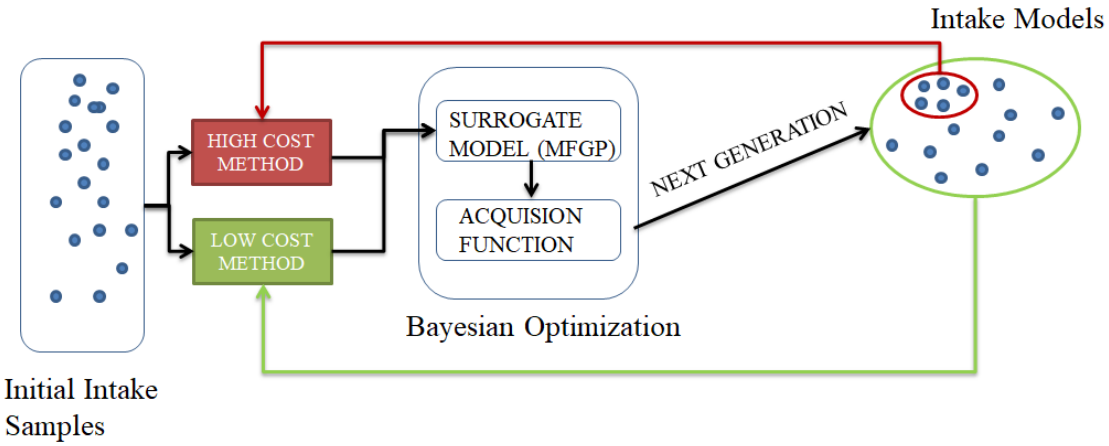

Figure 4.6: Schema of the Open Source Multi-Task Bayesian Optimization

Each initial sample analysis are applied with cross-validation to show surrogate model performance.

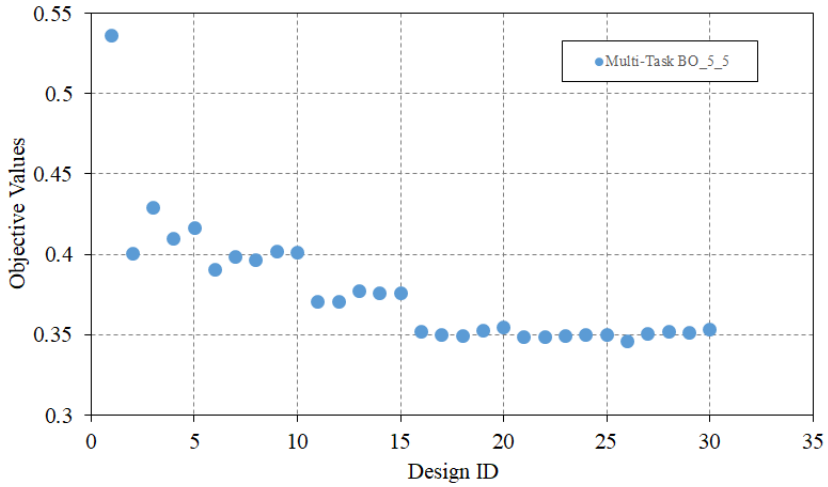

Figure 4.7: High Cost Objective History of Design ID over 5-5 Initial Sampling Multi-Task Bayesian Optimization

Only high cost objective values are plotted with respect to the design identity in Figure 4.7. Multi-tasking finds lower objective value in each cycle than in the previous cycle. Convergence occurs in 3 number of cycles and best fitness is 0.345 in terms of objective values.

Additionally, cross-validation analysis is applied for all high cost samples in optimization. As stated previously in section 2.4.2.2, converged hyper-parameters of

Gaussian process is used in the application of cross-validation. Leave one out cross-validation analysis details is given in Figure 4.8 for initial sampling 5-5 MTBO.

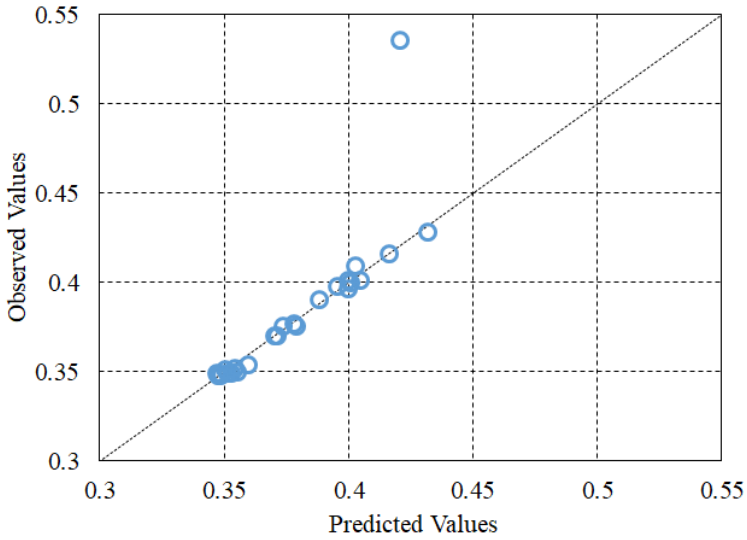

Figure 4.8: Cross-Validation Application for Initial Sampling 5-5 Bayesian Optimization.

The same optimization execution and cross-validation study is performed for 10 and 20 of number of initial size in Figure 4.9, 4.10, 4.11 and 4.12.

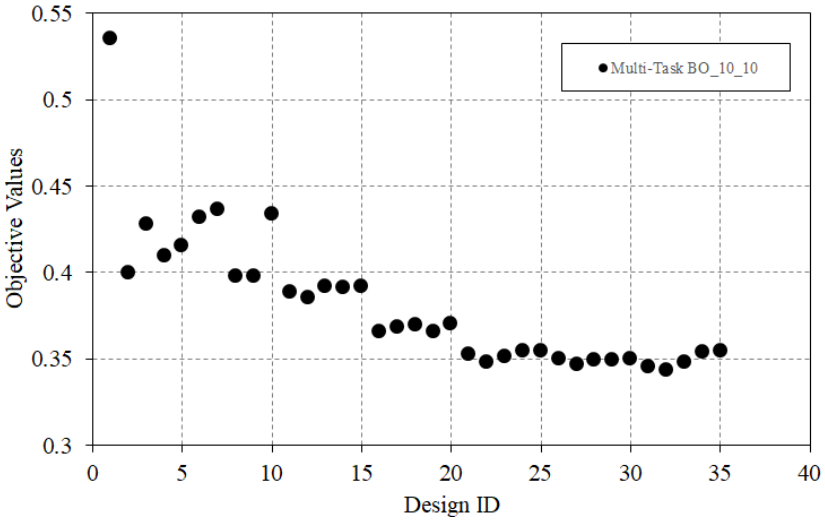

Figure 4.9: Objective History of High Cost Design ID over 10-10 Initial Sampling Multi-Task Bayesian Optimization

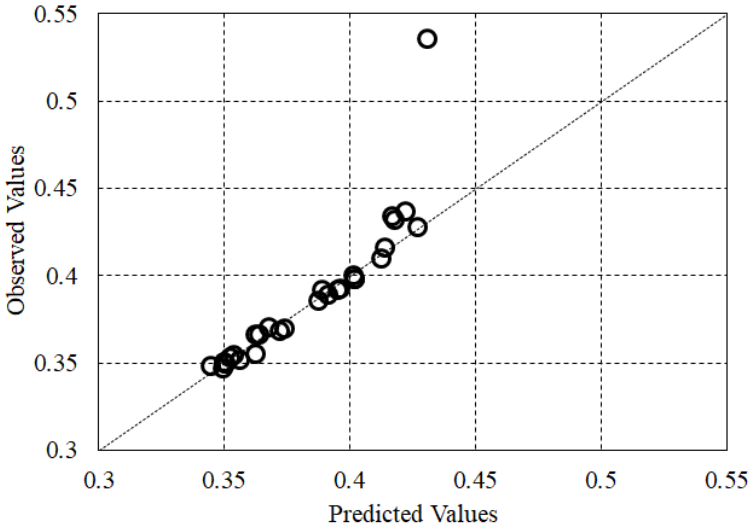

Figure 4.10: Cross-Validation Application for Initial Sampling 10-10 Bayesian Optimization.

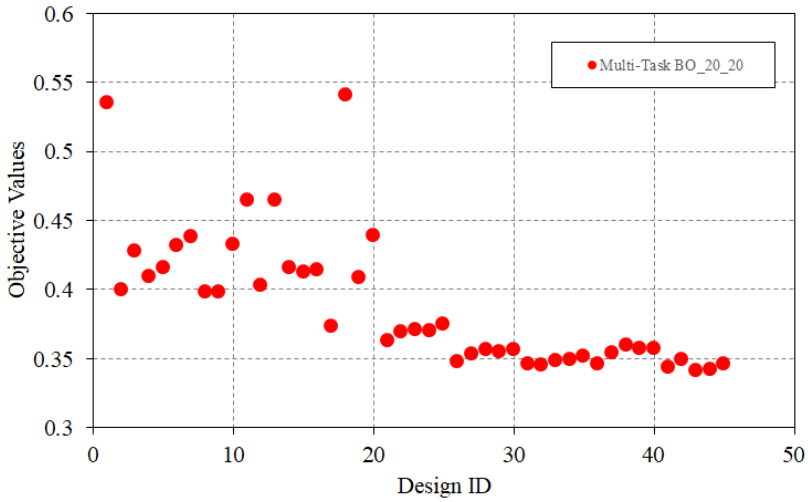

Figure 4.11: Objective History of High Cost Design ID over 20-20 Initial Sampling Multi-Task Bayesian Optimization

Cross-Validation analysis presented in Figure 4.12 shows that Gaussian Process performs better prediction on the lower objective values. The reason of scatter distribution around higher objective values is that surrogate model has fewer design points for regression. Optimization algorithm tries to minimize the objective function, therefore, new design points are generated with lower objective values. For this reason, having more points at low objective values improves surrogate model's success.

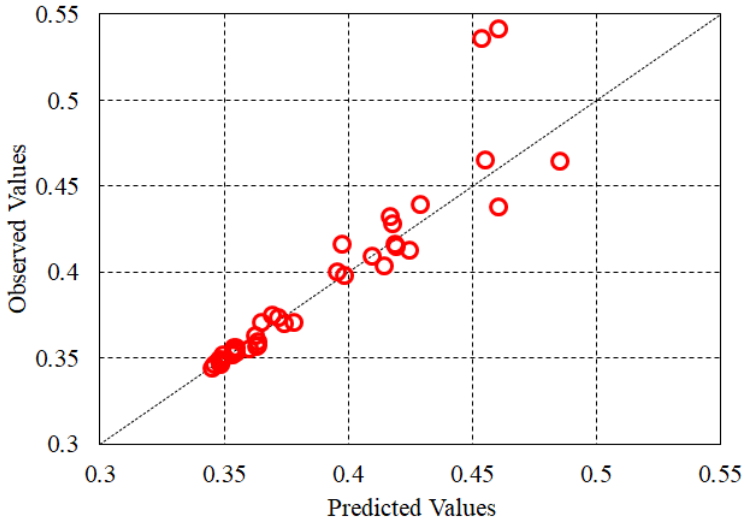

Figure 4.12: Cross-Validation Application for Initial Sampling 20-20 Bayesian Optimization.

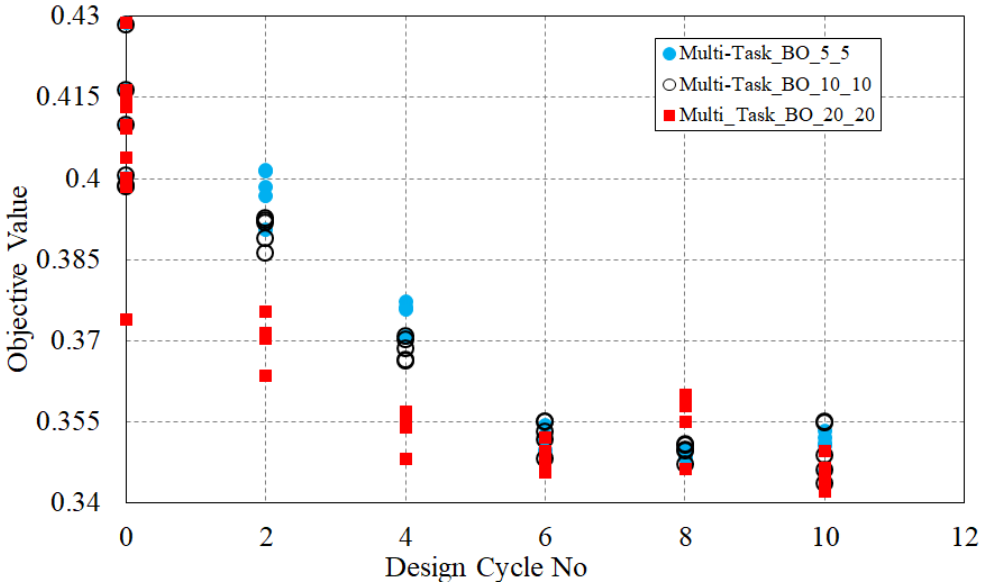

Figure 4.13: Comparison of Initial Sampling Size in terms of Objective Values with Arms.

In order to compare the effect of initial sampling size on convergence speed, optimization study has been performed for three different initial sampling size. The performance history of different design cycles is illustrated in Figure 4.13. Greater number of initial samples has faster convergence rate at initial design cycles. How-

ever, it is observed that sample size has minimal effect on the convergence rate and final objective value as design cycles increase.

In table 4.4, comparison of performance parameters that define the objective function are provided for three initial sample size. Although same level of objective values are obtained, differences between performance parameters are observed.

Table 4.4: Input Settings of Multi-Task Bayesian Optimization Application

Design ID	DC_{60}	PR	W-normalized	Objective Value
RAE-M2129	0.293	0.9744	0.59	0.420
5-5 MTBO	0.281	0.9902	0.62	0.344
10-10 MTBO	0.279	0.9850	0.61	0.344
20-20 MTBO	0.279	0.9912	0.65	0.343

Table 4.5 lists the parameters for the baseline and the improved intake. Significant changes occurred in y_3, y_5 and y_6 values which basically define the transition from inlet to interfacing plane.

Table 4.5: Input Details of Baseline and Optimized S-shape

Parameters	y1	y2	y3	y4	y5	y6	ΔL
Baseline Intake	136	125	82	56	13	1	0
Optimized Intake	135	125	70	60	30	10	4.91

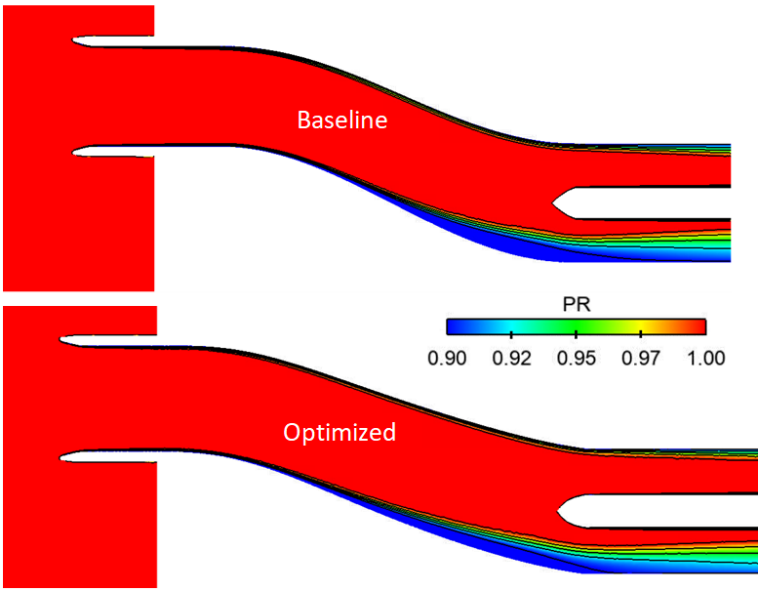

Figure 4.14: Total Pressure Ratio Comparison of Baseline and Best Design at Side-view.

Comparison of pressure recovery contours for baseline and optimized design point at mid-section is provided in Figure 4.14. Blue-color shows low pressure recovery region and red-color indicates high pressure recovery values. Total pressure losses is decreased for optimized design point.

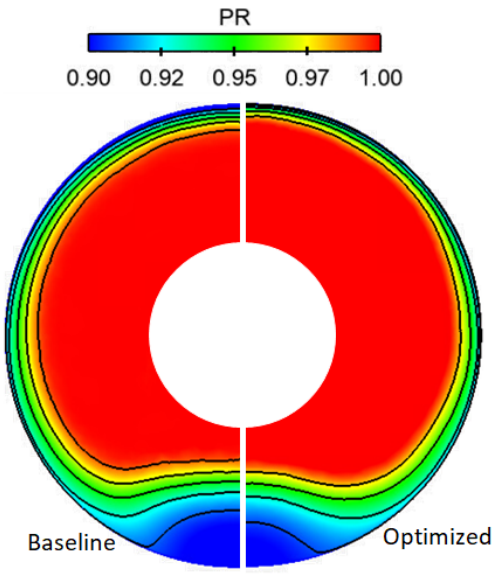

Figure 4.15: Total Pressure Ratio Comparison of Baseline and Best Design at AIP .

In order to better see the improvements, semi-images of AIP surface for baseline and optimum design points are combined in Figure 4.15. The level of losses are slightly reduced by using multi-tasking.

4.0.2 Comparison of Single Fidelity-Multi Fidelity Bayesian Optimization

Performance of optimization techniques for surrogate based Bayesian Optimization is examined with single task and multi task approaches. For single task approach, only high cost numerical analysis is used in Gaussian Process. Performance of methods are measured by how much time does it take for convergence of desired fitness. Figure 4.16 shows that elapsed time to reach same fitness for single-task approach is nearly 2 times slower than that for multi-task approach. Two approaches converge to similar objective values when convergence is achieved. Analysis takes nearly 1 hour for Spalart-Allmaras turbulence model and 3 hours for realizable k-ϵ turbulence model when 240 CPU Processors used in the cluster.

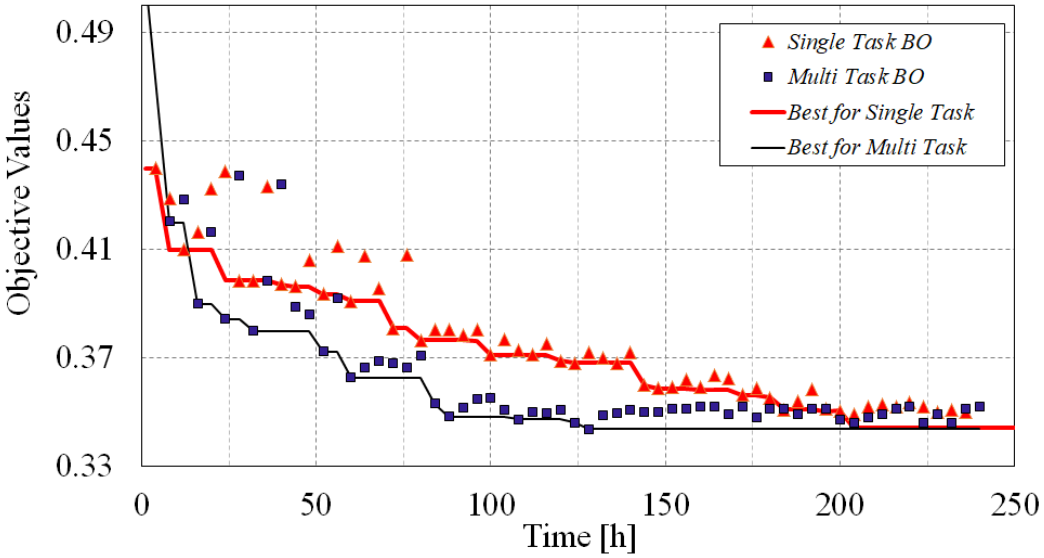

Figure 4.16: Single Task and Multi Task Comparison with respect to Elapsed Time

4.0.3 Parameters Relation on Objective Function

In this part, relation between performance parameters in design objective are investigated to understand physical characteristic of the S-duct. To look even more into

details, Pareto plots are drawn in Figure 4.17-4.18 and 4.19 . Data in 10-10 initial sampling with proper setting are used in those figures.

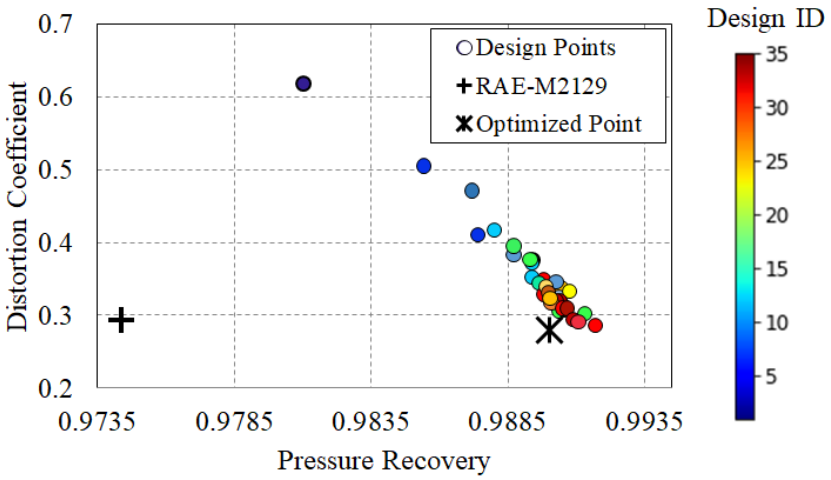

Figure 4.17: Parameters Comparison for Distortion Coefficients and Pressure Recovery of Design Points

Distortion coefficient and pressure recovery have negative strong correlation. It is observed that improvement on pressure recovery and distortion coefficient are correlated. Distortion coefficient is highly affected by secondary flows in the duct. Weaker secondary flows results in low distortion coefficient. Similarly, weaker secondary flow induces less pressure loss.

Pareto plot in Figure 4.18 shows the relation between the distortion coefficient and duct length.

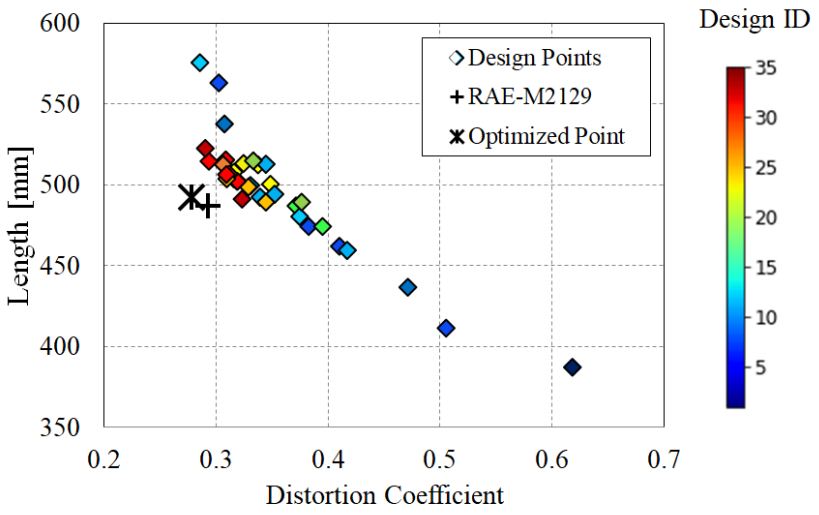

Figure 4.18: Parameters Comparison for Intake Length and Distortion Coefficient of Design Points

Normalized weight is directly influenced by the length of S-duct. Better distortion coefficient is obtained when length of S-duct gets longer. Long duct provide smoother transition from inlet to AIP, therefore, smaller separation regions are expected.

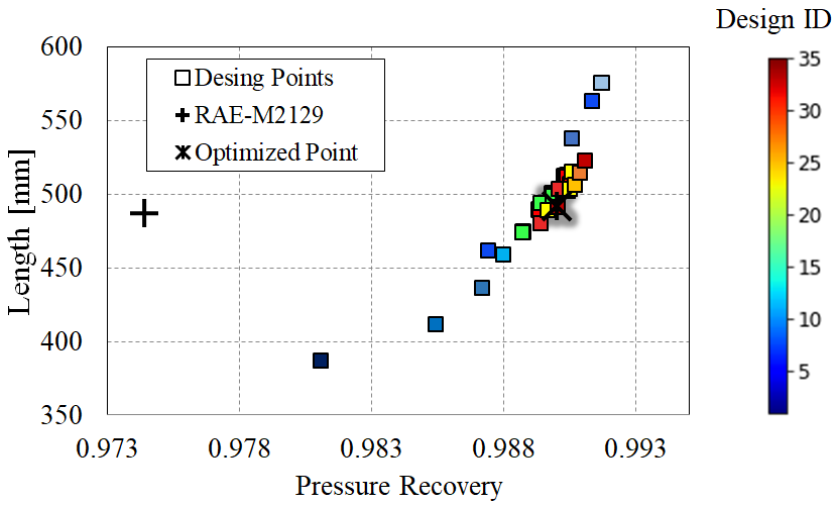

Figure 4.19: Parameters Comparison for Normalized Weight and Pressure Recovery of Design Points

The relation between the pressure recovery and duct length are shown in Figure 4.19. Pressure recovery values improve with increasing duct weight which is directly re-

lated to duct length. In fact, highest total pressure value is obtained at maximum weight. Longer duct length improves the flow quality through the duct. The similar relation is mentioned in the discussion of distortion coefficient-weight comparison.

To sum up, optimization structure can be visualized from Pareto plots. Parameter's relation shows that distortion coefficient and pressure recovery are affected in a similar manner by Length. Weight of S-duct behaves the inverse of these two parameters. Then, Bayesian optimization algorithm performs oscillatory selection for length of S-duct and that makes the system non-linear.

CHAPTER 5

CONCLUSION

In this thesis, the performance optimization of S-duct is improved by using machine learning based CFD optimization. Validation cases have been done for various cost of turbulence models. Unstructured mesh type is used for numerical analysis and boundary layer height is selected for proper y+ value to model turbulence. Grid convergence study is taken out for turbulence models. Also, RAE M-2129 intake model is taken as a validation model. Pressure Recovery, distortion coefficient, Mach Number and mass flow rate are compared at AIP plane with available experimental data [2]. Realizable k-ϵ turbulence model is selected for high cost model and Spalart- Allmaras is chosen for low cost model for Gaussian Process.

Bezier control points representing the RAE M-2129 geometry are taken as baseline input parameters. Then, the baseline input parameters are used to determine the bounds of Bezier parameters for optimization studies. Also, line continuity is taken into account when determining boundaries of the input parameters. The correlation calculation of the selected numerical methods is made within the limits of these input parameters. The Gaussian process is demonstrated with the given set of S-duct samples to predict the performance of another 5 intake models. A set of S-duct is analyzed by using correlated turbulence models to train the surrogate model. Bayesian application predicted perfectly and there are less than 1% differences between prediction values and high cost CFD results.

Different numbers of initial samples are used to investigate the effects on optimization. Higher number of initial sample has faster convergence on optimum design point. Also, the effect of the initial samples on optimization decreases in the further cycles of optimization. Input parameters of baseline and best design are tabulated and

pressure recover contours show the performance enhancement. Pressure recovery has increased by 1.5 %, and the distortion coefficient has dropped by 5%. The weight of an intake model, on the other hand, is increased by 6%.

Multi-task Bayesian optimization approach is compared with single-task Bayesian optimization. Multi-tasking has nearly two times faster convergence time than single-task optimization. Relation of performance parameters is investigated with related Pareto plots. There is a direct proportion between pressure recovery and distortion coefficient. Any geometrical changes that make the pressure recovery better, also decreases the distortion coefficient. As the length of the duct gets larger, the weight of an intake increases. Larger length size of an intake makes inlet flow much smoother. This improves pressure recovery and distortion coefficient, but the weight of the s-shape increases.

To sum up, multi-task Bayesian optimization has valuable influence on intake design. Due to requirement of extensive computational analysis, usage of cheap and expensive methods on Gaussian Process reduces global uncertainty. It also gives greater precision of prediction so that multi-task Bayesian optimization is crucial to project which has limited time and requires detailed analyses.

REFERENCES

[1] Meta Platforms Inc. Multi-task bayesian optimization. Available at `https://ax.dev/tutorials/multi_task.html` (2022).

[2] T. M. Berens, A. L. Delot, M. Chevalier, J. Van Muijden, R. A. Waaijer, and P. Tattersall. Application of cfd to high offset intake diffusers. *GARTEUR TP-173*, 2012.

[3] Boeing Inc. Agm-86b/c air launched cruise missile. Available at `https://www.boeing.com/history/products/agm-86b-c-air-launched-cruise-missile.page` (1998).

[4] J. C.R. Hunt, C. J. Abell, J. A. Peterka, and H. Woo. Kinematical studies of the flows around free or surface-mounted obstacles; applying topology to flow visualization. *Journal of Fluid Mechanics*, 86, 1978.

[5] V. H. Sahm and K. P. Werrell. The Evolution of the Cruise Missile. *Technology and Culture*, 28(2), 1987.

[6] C. Bajaj and G. Farin. Curves and Surfaces for Computer Aided Geometric Design–A Practical Guide. *Mathematics of Computation*, 55(192), 1990.

[7] Scikit-learn. Gaussian processes regressio. Available at `https://scikit-learn.org/0.17/auto_examples/gaussian_process/plot_gp_regression.html`.

[8] K. Swersky, R. P. Adams, and J. Snoek. Multi-Task Bayesian Optimization. *European Journal of Operational Research*, 270(3):1074–1085, 2018.

[9] I. Maghsoudi, M. Mahmoodi, and M. A. Vaziri. Numerical design and optimization of mechanical vane-type vortex generators in a serpentine air inlet duct. *European Physical Journal Plus*, 135, 2020.

[10] ONERA. Pressure rake for air inlet study. Available at https://www.onera.fr/en/windtunnel/flow-field-survey-and-visualization.

[11] G. B. Thomas, M. D. Weir, and J. Hass. *Thomas' calculus-13th*. 2013.

[12] T. M. Berens, A. L. Delot, M. Chevalier, and J. Van Muijden. Numerical Simulations for High Offset Intake Diffuser Flows. *52nd AIAA Aerospace Sciences Meeting - AIAA Science and Technology Forum and Exposition, SciTech 2014*, 2014.

[13] E. L. Fleeman. Tactical missile design second edition, 2006.

[14] J. Blazek. *Computational Fluid Dynamics: Principles and Applications: Third Edition*. Elsevier, 2015.

[15] O. Almeida, F.C. Miranda, N. O. Ferreira, and Saad F.G. Low Subsonic Wind Tunnel – Design and Construction. *Journal of Aerospace Technology and Management*, 10, 2018.

[16] P. Aref, M. Ghoreyshi, A. Jirasek, and M. J. Satchell. CFD Validation and Flow Control of RAE-M2129 S-Duct Diffuser using CREATE TM -AV Kestrel Simulation Tools. *Aerospace*, 5(1), 2018.

[17] S. Aslan and D. F. Kurtulus. *Numerical Investigation of an S-Duct Diffuser at Different Inlet Boundary Conditions*, pages 111–128. Springer International Publishing, Cham, 2018.

[18] N. Evstigneev. Integration of 3D Incompressible Free Surface Navier-Stokes Equations on Unstructured Tetrahedral Grid Using Distributed Computation on TCP/IP Networks. *WIT Transactions on Engineering Sciences*, 59:65–77, 2008.

[19] S. Guo, S. Huang, and M. Chi. Optimized Design of Engine Intake Manifold Based on 3D Scanner of Reverse Engineering. *Eurasip Journal on Image and Video Processing*, 2018(1), 2018.

[20] J. Volker. *Large Eddy Simulation of Turbulent Incompressible Flows*, volume 9. 2002.

[21] O. Reynolds. On the Dynamical Theory of Incompressible Viscous Fluids and the Determination of the Criterion. *Proceedings of the Royal Society of London*, 56(336-339), 1894.

[22] F. G. Schmitt. About Boussinesq's Turbulent Viscosity Hypothesis: Historical Remarks and A Direct Evaluation of its Validity. *Comptes Rendus - Mecanique*, 335(9-10):617–627, 2007.

[23] P. R. Spalart and S. R. Allmaras. One-Equation Turbulence Model for Aerodynamic Flows. *Recherche aerospatiale*, 1:5–21, 1994.

[24] N.E. May. Intake/s-bend diffuser flow prediction using linear and non-linear eddy-viscosity and second-moment closure turbulence models, 1999.

[25] O. Dababneh, T. Kipouros, and J. F. Whidborne. Application of an efficient gradient-based optimization strategy for aircraft wing structures. *Aerospace*, 5, 2018.

[26] T. A Wheeler M. J. Kochnderfer. *Algorithms for optimization*. The MIT Press, 2019.

[27] J. C. Spall. *Introduction to Stochastic Search and Optimization*. John Wiley and Sons, 2005.

[28] Alexander I. J. Forrester, András Sóbester, and Andy J. Keane. *Engineering Design via Surrogate Modelling*. 2008.

[29] M. Vlad E. Brochu and F.Nando. A tutorial on bayesian optimization of expensive cost functions, with application to active user modeling and hierarchical reinforcement learning, 2010.

[30] G. Harloff, B. Reichert, and S. Wellborn. Navier-Stokes Analysis and Experimental Data Comparison of Compressible Flow in a Diffusing S-Duct. In *10th Applied Aerodynamics Conference*, 1992.

[31] . H. Anderson and J. Gibb. Vortex-Generator Installation Studies on Steady-State and Dynamic Distortion. *Journal of Aircraft*, 35(4):513–520, 1998.

[32] P. R. Spalart, W. H. Jou, Mikhail Kh Strelets, and S. R. Allmaras. Comments on the Feasibility of LES for Wings and on a Hybrid RANS/LES Approach. *Advances in DNS/LES*, 1:4–8, 1997.

[33] R. E. Dadioti and S. Rees. Validation of a Detached Eddy Simulation (DES) Model in Complex Urban Environment. *Athens Journal of Sciences*, 3(2):113–136, 2016.

[34] A. Ahmed. Adjoint based aerodynamic shape optimization of subsonic submerged intake. Phd. Thesis, Middle East Technical University, 2021.

[35] M. Başaran. Adjoint-based design optimization of a hypersonic inlet. Master Thesis, Middle East Technical University, 2019.

[36] S. R. Wellborn, B. A. Wellborn, and T.H. Okiishi. Study of the Compressible Flow in a Diffusing S-Duct. *Journal of Propulsion and Power*, 10(5), 1994.

[37] N. Shojaee and H. Hazaveh. Investigation of Total Pressure Distribution at Aerodynamic Interface Plane of an " S-shaped " Air Intake at Sideslip Condition. *International Journal of Natural and Engineering sciences*, 6(3):87–94, 2012.

[38] G. Tanguy, D. Macmanus, E. Garnier, and P. Martin. Characteristics of Unsteady Total Pressure Distortion for a Complex Aero-engine Intake Duct To cite this version , volume = 78, year = 2020. *Aerospace Science and Technology*, pages 297–311.

[39] W. Zhang and M. Vahdati. A parametric study of the effects of inlet distortion on fan aerodynamic stability. *Journal of Turbomachinery*, 141(1), 2019.

[40] C. Zhang, B. Yang, Y. Wang, and G. Tu. Preliminary Research on a High Thrust-to-Weight Ratio of Double-Sided Composite Impeller Microturbine Engine. *International Journal of Aerospace Engineering*, 2021:1–27, 2021.

[41] R. M. Hicks and P. A. Henne. Wing Design By Numerical Optimization. *Journal of Aircraft*, 15(7):407–412, 1978.

[42] A. D. Belegundu and T. R. Chandrupatla. *Optimization Concepts and Applications in Engineering*. Prentice Hall, 2019.

[43] H. Kaya. Development of a discrete adjoint-based aerodynamic shape optimization tool for natural laminar flows. Phd. Thesis, Middle East Technical University, 2020.

[44] O. Akman. Subsonic-transonic submerged intake design for a cruise missile. Master Thesis, Middle East Technical University, 2014.

[45] M. Mitchell. *An Introduction to Genetic Algorithms*. MIT Press, Cambridge, 1996.

[46] E.Dinçer T. Ünlü, M. Atasoy and S. Eyi. Integrated shape optimization of rae-m2129 inlet for aerodynamic performance and reduced radar cross section. *AIAC Paper*, 2019.

[47] J. Kennedy and R. Eberhart. Particle Swarm Optimization. *Proceedings of IEEE International Conference on Neural Networks*, pages 1942–1948, 1995.

[48] J. Mockus. On the Bayesian Methods for Seeking the Extremal Point. *IFAC Proceedings Volumes*, 8(1):428–431, 1974.

[49] J. Mockus. *Global Optimization and the Bayesian Approach*. Kluwer Academic Publishers, Dordrecht, 1989.

[50] J. Mockus. Application of Bayesian Approach to Numerical Methods of Global and Stochastic Optimization. *Journal of Global Optimization*, 4(4), 1994.

[51] M. C. Kennedy and A. O'Hagan. Predicting the output from a complex computer code when fast approximations are available. *Biometrika*, 87, 2000.

[52] L. Parussini, D. Venturi, P. Perdikaris, and G. E. Karniadakis. Multi-fidelity Gaussian Process Regression for Prediction of Random Fields. *Journal of Computational Physics*, 336:36–50, 2017.

[53] D. Huang, T. T. Allen, W. I. Notz, and R. A. Miller. Sequential kriging optimization using multiple-fidelity evaluations. *Structural and Multidisciplinary Optimization*, 32(5), 2006.

[54] B. Letham and E. Bakshy. Bayesian Optimization for Policy Search via Online-Offline Experimentation. *Journal of Machine Learning Research*, 20, 2019.

[55] ANSYS Inc. ANSYS Fluent Theory Guide v19.3. *ANSYS 19.3 Documentation*, 2018.

[56] D.J. Tritton. *Physical Fluid Dynamics*. Cambridge University Press, 1976.

[57] D. C. Wilcox. *Turbulence modeling for CFD*. DCW Industries, 1993.

[58] W. P. Jones and B. E. Launder. The Prediction of Laminarization with a two-Equation Model of Turbulence. *International Journal of Heat and Mass Transfer*, 15(2), 1972.

[59] T. H. Shih, W. W. Liou, A. Shabbir, Z. Yang, and J. Zhu. A New K-epsilon Eddy Viscosity Model for High Reynolds Number Turbulent Flows: Model Development and Validation. *Computer & Fluids*, 24(August):227–238, 1995.

[60] F. R. Menter. Two-equation eddy-viscosity turbulence models for engineering applications. *AIAA Journal*, 32, 1994.

[61] D.R. Jones, M. Schonlau, and W. J. Welch. Efficient Global Optimization of Expensive Black-Box Functions. *Journal of Global Optimization*, 13(4), 1998.

[62] C. E. Rasmussen and C .K. I. Williams. *Gaussian Processes for Machine Learning*, volume 38. The MIT Press, 2006.

[63] J. Benesty, J.Chen, Y.Huang, and I. Cohen. Pearson correlation coefficient. in: Noise reduction in speech processing, 2009.

[64] H. Taherdoost. Sampling Methods in Research Methodology; How to Choose a Sampling Technique for Research. *SSRN Electronic Journal*, 2018.

[65] S. Burhenne, D. Jacob, and G. P. Henze. Sampling Based on Sobol Sequences for Monte Carlo Techniques Applied to Building Simulations. In *Proceedings of Building Simulation 2011: 12th Conference of International Building Performance Simulation Association*, 2011.

[66] A. B. Owen. Scrambling Sobol ' and Niederreiter Xing Points. *Journal of complexity*, 489:466–489, 1998.

[67] I. M. Sobol. On the Distribution Of Points In a Cube and the Approximate Evaluation of Integrals. *Zh. Vychisl. Mat. i Mat. Phys*, pages 86–112, 1967.

[68] M. Zhu H. Liang and Z. Wu. Using cross-validation to design trend function in kriging surrogate modeling. *AIAA Journal*, 52, 2014.

[69] T. Ünlü. Development of a design method for subsonic intakes with improved aerodynamic performance and reduced radar signature. Master Thesis, Middle East Technical University, 2021.

Appendix A

XChor Language - 1: Bezier Curve Python Scripts

```
def bezcurve(Xpoints,L,ino):
    def binomial(i,n):
        return math.factorial(n)/float(math.factorial(i) math.
            factorial(n i))
    def bernstein(t,i,n):
        return binomial(i,n) (t  i) ((1  t)  (n i))
    def bezier(t,controlpoints):
        n=len(controlpoints) 1
        x=y=0
        for i, pos in enumerate(controlpoints):
            bern=bernstein(t,i,n)
            x += pos[0]  bern
            y += pos[1]  bern
        return x,y
    def beziercurverange(n,points):
        for i in range(n):
            t=i/float(n 1)
            yield bezier(t,points)
    Rt=64.4
    Rf=76.2
    R=[]
    X=[]
    Y=[]
    Z=np.zeros(206)
    plt.close( all )
    P=Xpoints
    Bx=[]
    By=[]
    for point in beziercurverange(100,P):
        Bx.append(point[0])
        By.append(point[1])
    for i in range(0,len(Bx)):
        R.append(Rt+(Rf  Rt) (3 (1  Bx[i]/L)  4  4 (1  Bx[i]/L)  3+1))
    B=pd.DataFrame(columns=[ Bx , By ])
```

```
34      B.Bx=Bx[:]
35      B.By=By[:]
36       B.to csv( Bezier points.out ,index=False)
37       R=pd.DataFrame(data = R :R[:] ,dtype=np.float16)
38      X.append(Bx[0])
39      Y.append(By[0]+Rt)
40      X.append(Bx[0])
41      Y.append(By[0])
42      Z[1]=Rt
43      X.append(Bx[0])
44      Y.append(By[0] Rt)
45      X.append(Bx[0])
46      Y.append(By[0])
47      Z[3]= Rt
48      for i in range(1,len(Bx)):
49          X.append(Bx[i])
50          Y.append(By[i]+R[i])
51      X.append(Bx[ 1])
52      Y.append(By[ 1])
53      Z[len(Bx)+4 1]=Rf
54      X.append(Bx[ 1])
55      Y.append(By[ 1])
56      Z[len(Bx)+5 1]= Rf
57      X.append(Bx[ 1])
58      Y.append(By[ 1]+Rf)
59      X.append(Bx[ 1])
60      Y.append(By[ 1] Rf)
61      for i in range(1,len(Bx) 1):
62          X.append(Bx[i])
63          Y.append(By[i] R[i])
64      X.append(Bx[ 1])
65      Y.append(By[ 1] Rf)
66      Z1=Z.tolist()
67      data=np.column stack((X,Y,Z1))
68      np.savetxt( inlet geometry.dat ,data,delimiter= s ,fmt= f f
            f )
69      ppx,ppy=zip( P)
```

```
70      plt.xlim([0,700])
71      plt.ylim([ 100,200])
72      plt.plot(Bx,By)
73      plt.plot(ppx,ppy,marker= o ,linestyle=  )
74      plt.suptitle(f"Design ino ",x=0.2,y=0.3)
75      plt.xlabel( X [mm] )
76      plt.ylabel( Z [mm] )
77      plt.savefig( Curve +f"Design ino "+ .jpg )
78      plt.close()
79      return
```